A global simulation of tropospheric ozone and related tracers: Description and evaluation of MOZART, version 2

Larry W. Horowitz[1], Stacy Walters[2], Denise L. Mauzerall[3], Louisa K. Emmons[2], Philip J. Rasch[2], Claire Granier[4,5], Xuexi Tie[2], Jean-François Lamarque[2], Martin G. Schultz[6], Geoffrey S. Tyndall[2], John J. Orlando[2], and Guy P. Brasseur[6]

Submitted to *Journal of Geophysical Research,* August 16, 2002

Revised and resubmitted, November 2, 2002

1.Geophysical Fluid Dynamics Laboratory / NOAA, Princeton, New Jersey, USA
2.National Center for Atmospheric Research, Boulder, Colorado, USA
3.Woodrow Wilson School, Princeton University, Princeton, New Jersey, USA
4.NOAA Aeronomy Laboratory, Boulder, Colorado, USA
5.Service d' Aeronomie, University of Paris 6, Paris, France
6.Max Planck Institute for Meteorology, Hamburg, Germany

Abstract. We have developed a global three-dimensional chemical transport model called MOZART, version 2. This model, which will be released as a community model, is built on the framework of the NCAR MATCH transport model and can easily be driven with various meteorological inputs and model grids. In this work, we describe the standard configuration of the model, in which it is driven by meteorological inputs every 3 hours from the middle atmosphere version of the NCAR Community Climate Model (MACCM3), and uses a 20 minute timestep and a horizontal resolution of 2.8° latitude x 2.8° longitude with 34 vertical levels extending up to approximately 40 km. The model includes a detailed chemistry scheme for tropospheric ozone - nitrogen oxides - hydrocarbon chemistry, with 63 chemical species. Tracer advection is performed using a flux-form semi-Lagrangian scheme with a pressure fixer. Subgrid scale convective and boundary layer parameterizations are included in the model. Surface emissions include sources from fossil fuel combustion, biofuel and biomass burning, biogenic and soil emissions, and oceanic emissions. Parameterizations of dry and wet deposition are included. Stratospheric concentrations of several long-lived species (including ozone) are constrained by relaxation towards climatological values. The distribution of tropospheric ozone is well simulated in the model, including seasonality and horizontal and vertical gradients. However, the model tends to overestimate ozone near the tropopause at high northern latitudes. The global budget of tropospheric ozone is consistent with the range found in recent studies, but our production and loss rates are at the upper end of this range. The tropospheric production and loss of ozone is dominated by the tropics. Concentrations of nitrogen oxides (NO_x) and nitric acid (HNO_3) agree well with observed values, but PAN is overestimated by the model in the upper troposphere at several locations. Carbon monoxide (CO) is simulated well at most locations, but is slightly underestimated at some tropical stations. The

lifetime of methane (a useful measure of global abundance of OH) is 9.5 years (versus the recent IPCC estimate of 9.6 years). The simulated concentrations of non-methane hydrocarbons, and oxygenated intermediates (carbonyls and peroxides) generally agree well with observations.

1. Introduction

Ozone is of central importance in tropospheric chemistry. At high concentrations near the surface, it is harmful to humans and vegetation [*National Research Council*, 1991]. Photolysis of ozone, followed by reaction with water vapor, provides the primary source of the hydroxyl radical (OH), the primary atmospheric oxidant, in the troposphere [e.g., *Logan*, 1981]. In addition, ozone is a significant greenhouse gas, particularly in the cold upper troposphere [*Hansen et al.*, 1997]. Photochemical production of tropospheric ozone is catalyzed by nitrogen oxides (NO_x = NO + NO_2) during the oxidation of CO and hydrocarbons.

Several models of tropospheric ozone-NO_x-hydrocarbon chemistry have been developed and described recently [e.g., *Brasseur et al.*, 1998; *Lawrence et al.*, 1999; *Levy et al.*, 1999; *Lelieveld and Dentener*, 2000; *Bey et al.*, 2001]. There have been considerable differences among the models used in these studies, including in particular horizontal and vertical resolutions, emission inventories, chemical species and mechanism, meteorological fields, and method for calculating or specifying the stratosphere-troposphere exchange of ozone. The model we present in this work is highly flexible, has relatively fine horizontal and vertical resolution, and includes a fairly detailed representation of tropospheric ozone-NO_x-hydrocarbon chemistry, and includes updated emissions inventories. This model will be released as a community model, and will be available from NCAR/ACD at http://acd.ucar.edu/models/MOZART/. A detailed description of the model is provided in Section 2. Evaluation of model results is presented in Section 3. The simulated global and regional budgets of tropospheric ozone are discussed in Section 4. Discussion of the model results and conclusions are contained in Section 5. A detailed listing of the chemi-

cal mechanism used in MOZART-2 is provided in Appendix A.

2. Model description

MOZART-2 (Model of Ozone and Related Chemical Tracers, version 2) is a global chemical transport model designed to simulate the distribution of tropospheric ozone and its precursors. This model has been developed at multiple institutions, including the Atmospheric Chemistry Division (ACD) of NCAR, the NOAA Geophysical Fluid Dynamics Laboratory (GFDL), the Max Planck Institute (MPI) for Meteorology, and Princeton University. This version of the model includes significant updates and improvements to the chemistry, emissions, and transport over version 1 of the model [*Brasseur et al.*, 1998]. MOZART-2 simulates the concentrations of 63 chemical species (Table A1) from the surface up to the lower stratosphere. The model can be driven with a variety of meteorological inputs, including data from a general circulation model, such as the NCAR Community Climate Model (CCM), or a meteorological reanalysis, such as those from the National Centers for Environmental Prediction (NCEP) and the European Centre for Medium-Range Weather Forecasts (ECMWF). In the configuration described in this paper, MOZART-2 is driven with meteorological inputs (every three hours) from the middle atmosphere version of the CCM (MACCM3) [*Kiehl et al., 1998*]. In this version, the horizontal resolution is 2.8° latitude x 2.8° longitude with 34 hybrid vertical levels extending up to a pressure of 4 hPa (corresponding to an approximate altitude of 40 km), with a timestep of 20 minutes for all chemistry and transport processes. The meteorological fields from MACCM3 improve the representation of stratosphere-troposphere exchange versus the tropospheric version of CCM-2 (Ω 0.5 library) used in MOZART-1. Versions of the model driven by other dynamical inputs, which have been used in analysis and fore-

casting for field campaigns including TOPSE [*Emmons et al., 2002; Tie et al., 2002*], will not be discussed in this paper.

Meteorological parameters, including zonal and meridional winds, temperature, specific humidity, surface pressure, and surface fluxes of heat and momentum, are archived from an MACCM3 run and are provided to MOZART every three hours. MOZART is built on the framework of the transport model MATCH (Model of Atmospheric Transport and Chemistry) [*Rasch et al.*, 1997]. MATCH includes representations for advection, convective transport, boundary layer mixing, and wet and dry deposition. Convective mass fluxes are re-diagnosed by MATCH, using the *Hack* [1994] scheme for shallow and mid-level convection and *Zhang and MacFarlane* [1995] scheme for deep convection, as in (MA)CCM-3. The addition of a deep convective scheme provides more realistic rapid transport of trace species from the surface to the upper troposphere than in MOZART-1, which included only the *Hack* [1994] scheme. Vertical diffusion within the boundary layer is represented using the parameterization of *Holtslag and Boville* [1993]. Advection of tracers is performed using the flux-form semi-Lagrangian advection scheme of *Lin and Rood* [1996] with a pressure fixer as described in Section 2.4. The use of a flux-form advection scheme is a major improvement over the semi-Lagrangian scheme used in MOZART-1, in that it allows for tracer mass conservation and computes fluxes across grid-cell boundaries, which can be used in computing species budgets (as in Section 4). MOZART-2 uses only the lowest 34 vertical levels from MACCM3 (the full model has 52 levels extending up to 0.006 hPa). The additional MACCM3 layers in the upper stratosphere and mesosphere were found to be unnecessary for the simulation of tropospheric chemistry and transport (including stratosphere-troposphere exchange). Within the advec-

tion scheme, a rigid lid is imposed at the top of the MOZART-2 domain, and vertical velocities are re-diagnosed based on the continuity equation. This artificial imposition of a rigid lid at 4 hPa causes only a minor error in the re-diagnosed vertical velocities. Chemical species are updated each time step by a sequence of operators: advection, surface emissions and dry deposition, vertical diffusion, convection, and wet deposition and chemistry.

MOZART-2 is designed with a pre-processor that allows the model horizontal and vertical resolution, chemical species and reactions to be provided as input, and that generates the Fortran-90 source code based on these inputs. This allows considerable flexibility in specifying a model resolution, chemical mechanism, emissions, and also output variables. The chemical solver routines generated by the pre-processor allow the evolution of the chemical species in the model to be solved rapidly.

2.1 Chemistry

The chemical scheme used in MOZART-2 is considerably updated from that used in MOZART-1 [*Brasseur et al.,* 1998]. The chemical mechanism includes oxidation schemes for the non-methane hydrocarbons: ethane, propane, ethene, propene, isoprene, α-pinene (as a surrogate for all terpenes), and *n*-butane (as a surrogate for all hydrocarbons with 4 or more carbons, excluding isoprene and terpenes). A complete description of the kinetic and photochemical reactions used is provided in Appendix A.

Stratospheric concentrations of several long-lived species (O_3, NO_x=NO+NO_2, HNO_3, N_2O_5, and N_2O) are constrained by relaxation towards zonally and monthly averaged values from the middle atmosphere model STARS [*Brasseur et al.*, 1997] (for species other than O_3) and from “observed” ozone climatologies from *Logan* [2000] (for O_3

below 100 mb) and HALOE [*Randel et al.*, 1998] (for O_3 above 100 mb). This relaxation is performed from the local thermal tropopause (defined by a lapse rate of 2 K km^{-1}) to the model top at each timestep, with a relaxation time constant of 10 days. Concentrations of CH_4 and CO are also prescribed in the top two model levels (down to 6 hPa), based on model results from STARS.

2.2 Emissions

Surface emissions of chemical species in MOZART include those from fossil fuel burning and other industrial activity, biomass burning, biogenic emissions from vegetation and soils, and oceanic emissions. The emissions in MOZART are intended to be representative of those in the early 1990s. The surface emissions used in the model are summarized in Table 1. Monthly mean emissions of NO_x from various sources, for January and July, are shown in Figure 1. Biomass burning sources include forest burning, savannah burning, fuelwood use, and agricultural waste burning. Emissions from fossil fuel combustion, fuelwood burning, and agricultural waste burning are based on the EDGAR v2.0 inventory [*Olivier et al.*, 1996], with seasonality from the IMAGES model [*Müller, 1992*]. The spatial and temporal distribution of the amount of biomass burned is taken from *Hao and Liu* [1994] in the tropics, and from *Müller* [1992] in the extratropics. Emission ratios of chemical species from biomass burning are based on the recent review by *Andreae and Merlet* [2001]. Biogenic emissions of hydrocarbons from vegetation are taken from GEIA [*Guenther et al.*, 1995] for isoprene and monoterpenes, and from *Müller* [1992] for other species. The isoprene emissions in the tropics are reduced by 25% from the estimates of *Guenther et al.* [1995], based on more recent studies indicating that Guenther et al. [1995] may have overestimated isoprene emissions from tropical rainforests [e.g., *Klinger et al.*,

1998] (similar reductions in the tropics were included by *Bey et al.* [2001]). Biogenic emissions of methanol are included at an annual rate of 287 Tg/y based approximately on the emission ratio to isoprene found by *Guenther et al.* [2000] for North America, with spatial distribution and seasonality specified based on that used for higher hydrocarbons by *Müller* [1992]. Emissions of NO from microbial production in soils are taken from *Yienger and Levy* [1995], with soil emissions of CO, N_2O, and H_2 from *Müller* [1992]. Emissions of CO and hydrocarbons from the ocean are included in the model, with distributions as in *Brasseur et al.* [1998] but with reduced magnitudes (reduction factor is approximately 10 for alkanes, 4 for alkenes, and 2 for CO), based on more recent estimates. Oceanic emissions of acetone are also included, with a magnitude of 13.5 Tg/y, located primarily in the tropics (e.g., *Jacob et al.* [2002]). These emissions are available, at various horizontal resolutions, from the MOZART web site, http://acd.ucar.edu/models/MOZART/.

Lightning is distributed in the model according to the location of convective clouds, as diagnosed by the MATCH scheme. The corresponding source of NO_x is parameterized following *Price et al.* [1997], with a “C-shaped” vertical profile [*Pickering et al.*, 1998]. According to the *Price et al.* [1997] parameterization, the lightning frequency depends strongly on the convective cloud top height, and the ratio of cloud-to-cloud vs. cloud-to-ground lightning depends on the cold cloud thickness (from 0°C to the cloud top). The lightning source is scaled to provide a total of 3.0 TgN (as NO) per year, with significant diurnal and seasonal fluctuations based on the model meteorology. The value of 3.0 TgN/y used in this study is within the range of 3-5 TgN/y estimated by *Levy et al.* [1996], but is well below the range of 5-20 TgN/y estimated by *Price et al.* [1997]. Most

recent global modelling studies have used NO_x sources from lightning in the range of 3-7 TgN/y [e.g., *Brasseur et al.*, 1998; *Levy et al.*, 1999; *Lelieveld and Dentener*, 2000; *Bey et al.*, 2001]. Aircraft emissions of NO_x and CO are included in the model, based on *Friedl* [1997], with magnitudes of 0.67 TgN/y (NO) and 1.44 Tg/y (CO).

2.3 Dry Deposition and Wet Scavenging

Dry deposition velocities are included in the model for O_3, HNO_3, NO_2, CO, H_2O_2, organic hydroperoxides, carbonyl compounds, HO_2NO_2, PANs and other organic nitrates, alcohols, CH_4, NO, Pb, and H_2. They are calculated off-line using a resistance-in-series scheme [*Wesely*, 1989; *Hess et al.*, 2000] driven by 10 years of meteorological fields from NCEP reanalyses every 6 hours. The monthly mean of the calculated values are then computed and used in the model. The calculation of surface resistances uses the vegetation distribution of *DeFries and Townshend* [1994]. The calculation is done on a 1°x1° grid, and then averaged to the model resolution taking into account the different vegetation types within each grid cell. A diurnal cycle is imposed on the monthly mean deposition velocity for O_3 as in *Brasseur et al.* [1998].

Wet deposition is represented as a first-order loss process within the chemistry operator, with loss rates computed based on the large-scale and convective precipitation rates diagnosed by MATCH. Soluble species -- HNO_3, H_2O_2, CH_2O, organic hydroperoxides (CH_3OOH, C_2H_5OOH, C_3H_7OOH, POOH, ROOH, ISOPOOH, MACROOH, XOOH), CH_3COOOH, CH_3COCHO, HO_2NO_2, alkyl nitrates (ONIT, ONITR, $ISOPNO_3$), MVK, MACR, GLYALD, HYAC, CH_3CHO, alcohols (CH_3OH and C_2H_5OH), and Pb -- undergo wet removal by in-cloud scavenging, using the parameterization of *Giorgi and Chameides* [1985]. In addition, highly soluble species (HNO_3, H_2O_2,

ONIT, ISOPOOH, MACROOH, XOOH, Pb) are also removed by below-cloud washout, using the formulation described in detail by *Brasseur et al.* [1998]. The wet deposition scheme used here differs from that used in MOZART-1 in that in-cloud removal of highly soluble species is treated using the *Giorgi and Chameides* [1985] parameterization rather than the *Brasseur et al.* [1998] scheme as was done in MOZART-1. This change considerably increases the wet removal of these species, and greatly improves agreement of HNO_3 concentrations and wet deposition fluxes with observations (see Section 3.2).

2.4 Pressure fixer

Mass consistency problems with advection schemes in offline tracer transport models in general, including the *Lin and Rood* [1996] scheme, lead to non conservation of tracer mass. This effect results from the inconsistency between the vertically integrated mass convergence computed by the advection scheme and the surface pressure tendency interpolated from the dynamical input files. A more complete discussion of this issue is provided by *Jöckel et al.* [2001]. The pressure fixer developed by P. Cameron-Smith at LLNL [P. Cameron-Smith, personal communication, 2002; http://asd.llnl.gov/pfix/] is used in MOZART-2 to modify the horizontal mass fluxes so as to achieve consistency with the surface pressure tendency archived from the MACCM, eliminating the problem of mass inconsistency and tracer non conservation. The pressure fixer typically imposes only a small change on the horizontal wind fields, and does not alter large-scale circulation features. If the pressure fixer in MOZART-2, running with MACCM3 meteorological inputs, this non conservation would produce an anomalous source of ozone in the vicinity of the tropopause (where the vertical gradient of the ozone mixing ratio is large) of approximately 187 Tg/y (87 Tg/y of this total is within the troposphere, as defined in the budget

analysis in Section 4).

3. Model evaluation

The model is driven by meteorology from the MACCM3 general circulation model. This meteorology is intended to simulate a "typical" year, not any specific year of observations. In order to compare model results with observations, a multiyear climatology throughout the troposphere would be desirable. Such a climatology is only available at a large number of sites for ozone, based on long-term ozonesonde measurements, as compiled by *Logan* [1999]. For ozone, we compare monthly (or seasonal) mean model results with the corresponding multiyear mean observations. For other species, such as CO, NO_x, PAN, HNO_3, acetone, H_2O_2, and NMHCs, we compare model results with observations obtained from aircraft campaigns, as compiled by *Emmons et al.* [2000]. For these species, we compare mean regional vertical profiles observed during a given field campaign with model results averaged over the same geographical region and time period. A detailed description of the method used to construct the observed regional mean profiles from the raw observations is given by *Emmons et al.* [2000]. For CO, we also compare model results with multi-year surface observations from the NOAA/CMDL flask measurement network [*Novelli et al.*, 1998]. Additional comparisons between MOZART-2 model results and observations are available on the MOZART web page located at http://acd.ucar.edu/models/MOZART/.

3.1 Ozone

3.1.1 Vertical profiles

The modeled monthly mean concentrations of ozone near the surface and at 500 hPa are shown (for January and July) in Figure 2. Ozone concentrations at northern mid-

latitudes increase dramatically from January to July near the surface (and to a lesser extent in the middle troposphere), as a result of photochemical production of ozone, which requires high concentrations of NO_x and other precursors, as well as ultraviolet radiation. In biomass burning regions of South America and southern Africa, an increase in near-surface ozone can also be seen from January to July, reflecting the seasonal cycle of biomass burning, which provides the precursors for ozone production. Ozone concentrations generally increase with height, outside of regions of strong ozone production near the surface. This results from subsidence of ozone-rich air from the upper troposphere and the stratosphere.

Simulated vertical profiles of ozone are compared with ozonesonde observations in Figure 3. The observations are from multiple years of sonde measurements, as compiled by *Logan* [1999]. The simulated magnitude and vertical gradient of ozone are generally in good agreement with observations. At tropical and sub-tropical locations (e.g., Hilo, Brazzaville, Natal, and Samoa), the model simulates well the observed magnitude and vertical structure of ozone, including relative maxima in many of the profiles in the lower to middle troposphere above the boundary layer. At high northern latitudes, the model tends to overestimate ozone in the vicinity of the tropopause at several sites by 25% or more (e.g., Alert, Churchill), particularly in winter. The observations in the tropopause region at these stations tend to show large variability, probably indicating large variations in tropopause height. The model may not adequately resolve the location of the tropopause. The model overestimate of ozone in this region may also result in part from excessive cross-tropopause transport of ozone by advection at these latitudes in the model. The agreement with observations is generally better at northern mid-latitudes (Cape Kennedy and Hohenpeis-

senberg), although discrepancies remain at certain stations (e.g., Kagoshima). The agreement between simulated and observed ozone is improved considerably from that obtained with MOZART-1 [*Hauglustaine et al.*, 1998], in which tropospheric ozone was systematically too low, particularly at high latitudes and high altitudes. This improvement results from a variety of improvements to the model, in particular the advection scheme, the dynamical inputs, stronger convective transport to the upper troposphere, and improved chemical scheme and emissions.

3.1.2 Seasonal variation

The seasonal variation of simulated ozone mixing ratios at three pressure levels (800 hPa, 500 hPa, and 300 hPa) is compared with observations in Figure 4. At 800 hPa, the simulated seasonal cycle of ozone agrees well with observations at most sites. Northern mid-latitude sites tend to show a seasonal maximum during spring to summer at this level (e.g., Hohenpeissenberg), reflecting the seasonal cycle of photochemical ozone production and possibly stratospheric influence. The model simulates this general feature of the observations, but shifts the maximum several months too late at Wallops Island. In the southern tropics (e.g., Ascension Island), the observations indicate peak ozone concentrations during July-September (depending on location), reflecting the combined influences of biomass burning emissions and dynamics [*Moxim and Levy*, 2000]. The model tends to reproduce approximately the timing and the magnitude of this maximum.

In the mid-troposphere, at 500 hPa, the seasonal maximum of ozone at northern extratropical sites typically occurs in the late spring (May-June). The model reproduces this feature at most sites. However, ozone at Resolute is overestimated by about 20% throughout much of the year. This overestimate results in part from excessive downward

transport from the upper troposphere at high northern latitudes in the model (as discussed in the previous section).

In the upper troposphere, at 300 hPa, the model captures the observed seasonality of ozone at most sites. As mentioned in the previous section, the model tends to overestimate ozone near the tropopause at some sites at northern middle to high latitudes, such as at Hohenpeissenberg, where ozone is overestimated by 25-50% in some months.

3.2 Nitrogen species

Simulated monthly mean concentrations of NO_x are shown in Figure 5. High NO_x concentrations are present near the surface over regions with strong emissions of NO_x from fossil fuel combustion (e.g., North America and Europe), biomass burning (South and East Asia, South America, Africa), or other sources. The seasonal cycle of NO_x near the surface may be controlled by the seasonality of emissions (especially in the case of biomass burning), or by chemistry and transport (e.g., over North America, where chemical loss is slower during the winter, as is the ventilation of the continental boundary layer). Mid-tropospheric NO_x concentrations reflect transport from surface sources, as well as in situ production from lightning (see Section 2.2). Comparisons of simulated and observed vertical profiles of NO_x, PAN, and HNO_3 are shown in Figures 6-8, respectively. The regions used for these profile comparisons are listed in Table 2.

Predicted NO_x concentrations are generally in very good agreement with the observed values, given the large spatial and temporal variability in this short-lived species. The model overestimates values near the surface over some island locations, e.g., Japan_Coast_E in PEM-West-A/B and Hawaii in PEM-Tropics-B (not shown), because

terrestrial emissions are spread throughout the entire model gridbox, while the measurements may sample the clean marine boundary layer. Good agreement with observations is seen in the upper troposphere at all locations except New Zealand (in PEM-Tropics-A, not shown), suggesting that the source of NO_x from lightning in MOZART is approximately correct.

Concentrations of PAN in the model tend to increase strongly with altitude at most sites, with maximum mixing ratios appearing in the upper troposphere. This reflects the very long thermal decomposition time of PAN in the cold upper troposphere, and the slow loss by photolysis (with a lifetime of about a month). PAN is either transported to the upper troposphere by rapid convection, or is formed there by reactions of its precursors, hydrocarbons (which are transported to the upper troposphere by convection) and NO_x (which has a strong upper tropospheric source from lightning). These profiles agree with observations at many sites, although there are a significant number of regions at low to middle latitudes (e.g., the PEM-West-A regions, and Christmas Island in PEM-Tropics-A, and Tahiti and Fiji in PEM-Tropics-B), in which the model overestimates PAN concentrations in the upper troposphere by a factor of 2. Note that these significant overestimates occur in regions in which the observed upper tropospheric PAN concentrations are quite low (typically < 50 pptv). The overestimate in these regions may be due to excessive convective transport of PAN precursors accompanied by NO_x production from lightning. This is supported in some cases by comparisons of other species. For instance, MOZART also overestimates CO and C_3H_8 in the upper troposphere over Fiji during PEM-Tropics-B (see Section 3.3 and 3.4). In regions with higher observed PAN concentrations, by contrast, the model shows much better agreement with observations.

Simulated concentrations of HNO_3 are in reasonable agreement with observations at most locations. The HNO_3 concentrations in MOZART-2 are highly sensitive to the parameterization of wet deposition. For instance, if we were to use much slower wet deposition rates for HNO_3 (e.g., by using the wet deposition formulation used by *Hauglustaine et al.* [1998] in MOZART-1), HNO_3 concentrations would be overestimated by a factor of 2 or more at most locations. The wet deposition fluxes of HNO_3 from MOZART-2 agree with the observations (compiled by *Dentener and Crutzen* [1994]) to within a factor of two at most stations (Figure 9). There is a significant systematic overestimate of wet deposition only for the South Asian region, where the model is generally high by more than a factor of two. Many other current global 3-D models have reported overestimating HNO_3 concentrations at many locations throughout the troposphere [*Hauglustaine et al.*, 1998; *Mickley et al.*, 1999; *Bey et al.*, 2000]. These studies generally attribute this overestimate to several causes, including inaccurate representation of wet deposition, neglecting partitioning of nitrate into the aerosol phase (whereas the observations include only the gas-phase nitric acid), and possible missing reactions to convert HNO_3 back to NO_x. We find no such systematic error in HNO_3 concentrations or wet deposition fluxes in MOZART-2.

3.3 Carbon monoxide

Monthly mean concentrations of CO predicted by the model are shown in Figure 10. High concentrations of CO are found near the surface over regions with large emissions from biomass burning or fossil fuel combustion. Over industrial regions, surface CO concentrations are highest during winter, reflecting the slow chemical loss and decreased ventilation of the boundary layer. During summer, OH concentrations increase dramatically, and background concentrations of CO over the ocean surface decrease considerably.

In the tropics, the seasonality of CO concentrations also depends strongly on the seasonality of biomass burning, which account for over half of the direct emissions of CO.

Surface CO mixing ratios are compared with observations at selected measurement sites in Figure 11. Simulated CO concentrations and seasonal cycles agree well with observations at most of the observation sites. In the tropics, the simulated seasonal cycle agrees closely with observations at most sites, while there is a tendency for the simulated concentrations to be too low by 10 ppbv or more in some months. The seasonal maximum at Christmas Island is delayed by 3 months relative to the observations, possibly indicating a problem with the timing of biomass burning, or a problem with transport in the model (such as a poorly located ITCZ). At several sites at high northern latitudes (Alert and Barrow), the model underestimates the observed seasonal cycle, while simulating the mean concentration well. This problem, together with the underestimate of CO in the tropics, may result from problems with the spatial or seasonal distribution of the hydroxyl radical (OH) in our model, or may reflect problems with the biomass burning seasonal cycle. A similar underestimation of the seasonal cycle at high northern latitudes by *Holloway et al.* [2000] was attributed to unrealistically strong downward transport from the lower stratosphere, insufficient mixing of CO from lower latitudes, and emissions of CO from fossil fuel combustion that were too low. At the extratropical sites in the southern hemisphere, MOZART simulates the observed CO concentrations and seasonal cycle well. *Bey et al.* [2001] noted that their model underestimated CO concentrations at most locations. MOZART-2 does not show such a global bias (except for the slight underestimate in the tropics), but the total direct emissions of CO in our model are about 25% higher than those used by *Bey et al.* [2001].

Simulated regional vertical profiles of CO are compared with observations in Figure 12. Carbon monoxide concentrations predicted by the model agree with observations to within 10 ppbv at most sites, and generally capture the observed vertical gradients. At a few locations, however, the model overestimates observations by more than 10 ppbv, (Hawaii, PEM-Tropics-A, not shown), or underestimates observations by more than 10 ppbv (Philippine Sea and Pacific_Tropics_W (not shown), PEM-West-A). In the previous section, the model was shown to agree well with CO at Mauna Loa, Hawaii during the August-October season during which PEM-Tropics-A was conducted, but to slightly underestimate the observations at Christmas Island during these months. However, the model overestimates the observations from PEM-Tropics-A over both of these regions (comparison with Hawaii region not shown). This may indicate atypical transport patterns or biomass burning emissions during the period of this campaign.

3.4 Non-methane hydrocarbons

Simulated regional vertical profiles of the hydrocarbon ethane are compared with observations in Figure 13. The model simulates observed mean concentrations for ethane to within ±25% at most locations. The model results for propane (not shown) compare similarly well with observations. As with CO, however, the model underestimates concentrations of both of these hydrocarbons in the Philippine Sea and Pacific_Tropics_W (not shown) regions (PEM-West-A). The simultaneous underestimate of CO and ethane and propane in these regions may either indicate a missing emission source in or upwind of these regions, or a transport problem in the model, which causes inadequate transport of pollution to this region during the September-October period. There is also an underestimate of the alkanes in the East Atlantic region (SONEX).

3.5 Oxygenated species

Formaldehyde is a key intermediate in the oxidation of methane and many non-methane hydrocarbons in the troposphere. Formaldehyde is lost primarily through photolysis and reaction with OH. Photolysis of formaldehyde provides an important source of HO_x radicals in the troposphere. Comparisons of simulated and observed regional vertical profiles of formaldehyde are shown in Figure 14. In the regions with the most extensive observations, PEM-Tropics-B and some of the TRACE-A regions, the model simulates the observed concentrations of formaldehyde well. In other regions, e.g., Africa_Coast_W and Atlantic_S (TRACE-A), the model shows large disagreements with the observations. In these regions, however, the few available observations may not adequately represent the regional abundance of this short-lived species.

Acetone has surface emissions from anthropogenic sources, biomass burning, and vegetation [*Jacob et al.*, 2002]. We have also included a speculative oceanic source of acetone, based on recent observational and modelling studies [*Singh et al.*, 2001; *Jacob et al.*, 2001]. Acetone also has a large secondary source in the troposphere from oxidation of non-methane hydrocarbons, primarily propane. Acetone has a tropospheric lifetime ranging from less than a month to several months. Photolysis of acetone is an important source of HO_x radicals in the upper troposphere [*Jaeglé et al.*, 2001]. Vertical profiles of acetone from the model and observations are compared in Figure 15. In most of the regions (including those from the TRACE-A, PEM-West-B, and SONEX campaigns), the model estimates of acetone agree reasonably well with observations. The observations in PEM-Tropics-B indicate surprisingly large abundances of acetone over the tropical Pacific [*Singh et al.*, 2001], a region where most models predict quite low acetone concentrations

[e.g., *Bey et al.*, 2001; *Hauglustaine et al.*, 1998]. These observations suggest the presence of a large natural, distributed source of oxygenated organic species, as was found by *Jacob et al.* [2001]. Recent oceanic observations suggest that photochemical production of acetone in the surface ocean may provide a source of atmospheric acetone [*Zhou and Mopper*, 1997]. The addition of an ocean source of acetone in MOZART-2 improves the agreement between simulated and observed concentrations, but the model still underestimates acetone by up to a factor of 2 in the Tahiti and Easter Island (not shown) regions (PEM-Tropics-B). A stronger oceanic source of acetone, as suggested by *Jacob et al.* [2001] (27 Tg/y), may improve the agreement with observations in these regions, but was rejected in this study because it led to an even larger overestimate of PAN concentrations in the upper troposphere (see Section 3.2).

Hydroperoxides are formed in the atmosphere by permutation reactions between peroxy radicals. Self-reaction of HO_2 forms hydrogen peroxide (H_2O_2), while reaction of CH_3O_2 with HO_2 forms methylhydroperoxide (CH_3OOH). These reactions are the main sinks for HO_x radicals in much of the troposphere. Because of this coupling between HO_x radicals and hydroperoxides, evaluation of simulated concentrations of H_2O_2 and CH_3OOH provide an indirect test of the model simulation of HO_x. An important difference between the behavior of H_2O_2 and CH_3OOH in the troposphere is based on their solubility. H_2O_2 is much more soluble than CH_3OOH, and so can be removed readily by wet deposition. Because of its relatively weak solubility, CH_3OOH can be convected to the upper troposphere, where it may provide an important source of HO_x [*Prather and Jacob*, 1997]. Simulated concentrations of H_2O_2 and CH_3OOH are shown in Figures 16 and 17, respectively. The model simulates observed concentrations and vertical gradients of these

species very well in most regions. One exception is the overestimate of the hydroperoxides in the lower troposphere by more than a factor of 2 in the East Atlantic and Newfoundland (not shown) regions (SONEX). The model underestimates H_2O_2 by 20-50% in the lower troposphere in the Philippine Sea and Pacific_Tropics_W (not shown) regions during the PEM-West-A campaign; the model similarly underestimates CH_3OOH by about 25% in these regions.

3.6 Hydroxyl radical

The hydroxyl radical (OH) is the primary oxidant in the troposphere, and is responsible for the removal of many reduced compounds from the atmosphere. The zonally and monthly averaged distributions of OH are shown in Figure 18. Concentrations of OH are highest in the lower to middle troposphere in the tropics, and in northern midlatitudes during summer. The simulated OH concentrations are similar to those computed by *Spivakovsky et al.* [2000], and generally agree with those estimates at most locations and seasons to within 10-20%.

The lifetime of methane versus reaction with tropospheric OH provides a measure of the overall abundance of OH in the troposphere (with an emphasis on the tropical lower troposphere, where the warm temperatures allow the $OH+CH_4$ reaction to proceed quickly). In our model, the methane lifetime versus tropospheric OH (defined as the atmospheric methane burden divided by the annual sink of methane by reaction with OH in the troposphere) is 9.5 years. The total methane burden is 4630 Tg (tropospheric burden, 3930 Tg), and the tropospheric sink by reaction with OH is 488 Tg/y (loss to OH in the stratosphere, 16 Tg/y). The 2001 IPCC report [*Prather et al.*, 2001] estimated a sink versus tropospheric OH of 507 Tg/y, with a corresponding lifetime of 9.6 years (total lifetime

including other loss processes, 8.4 years). These figures suggest that the global tropospheric OH concentrations in MOZART-2 are consistent with the estimate by IPCC. The methane lifetime in our model is quite sensitive to the wet deposition parameterization, which can remove odd-hydrogen reservoirs such as peroxides from the atmosphere, and to the distribution of water vapor (input from MACCM3), which controls an important source of odd-hydrogen in the troposphere. The OH abundance is also sensitive to photolysis rates, which are computed in the model from a lookup table.

4. Ozone budget

The budget of tropospheric ozone in MOZART is shown in Table 3. The budget is calculated for odd oxygen, defined as $O_x = O_3 + O(^1D) + O(^3P) + NO_2 + 2\times NO_3 + 3\times N_2O_5 + HO_2NO_2 + HNO_3 + PAN + MPAN$ to account for chemical recycling within this family of species. Ozone is the most abundant member of this chemical family, so the budget for O_x can be interpreted as a budget of ozone. Photochemical production of O_x results primarily from the reaction of NO with hydroperoxy radicals or organic peroxy radicals to form NO_2. The NO_2 photolyzes to form $O(^3P)$, which rapidly reacts with O_2 to form ozone. Photochemical loss of O_x occurs mainly through the reaction of $O(^1D)$ (from O_3 photolysis) with H_2O to form 2 OH radicals, the reaction of ozone with OH and HO_2, and the ozonolysis of unsaturated hydrocarbons.

The photochemical production and loss of ozone in the troposphere are estimated by MOZART to be 5258 Tg y^{-1} and 4749 Tg y^{-1}, respectively. These terms dominate over the net stratospheric input of 343 Tg y^{-1}. The stratospheric input estimated by the model consists mostly of net advection of ozone across the tropopause (334 Tg y^{-1}), with a small contribution from convection and vertical diffusion (9 Tg y^{-1}). The loss of ozone by dry

deposition at the surface is 857 Tg/y. In an earlier version of MOZART-2, not using the LLNL pressure fixer, there was also a significant contribution (87 Tg y^{-1}) to the tropospheric ozone budget resulting from mass consistency corrections in the advection scheme, as discussed in Section 2.4 and *Jöckel et al.* [2001],

The photochemical production and loss rates of ozone estimated here are much larger than the values obtained with MOZART-1 [*Hauglustaine et al.*, 1998; *Hauglustaine and Brasseur*, 2001]. These earlier studies only computed ozone budgets up to 250 hPa, while we extend the budget domain up to 100 hPa in the tropics. Even if we restrict the MOZART-2 budget domain to 250 hPa, the photochemical production and loss terms still exceed the values of *Hauglustaine and Brasseur* [2001] by 30% and 73%, respectively. The MOZART-1 production and loss rates, however, were quite low compared with estimates from other model simulations. The more rapid ozone photochemistry in MOZART-2 results in part from the inclusion of the *Zhang and MacFarlane* [1995] deep convection scheme, which rapidly transports emitted species to the middle and upper troposphere increasing photochemical activity there, as well as from the 15% increase in total surface NO_x emissions. The values obtained in the present study fall approximately within the range obtained by recent studies, which is 3018-4900 Tg y^{-1} for production, and 2511-4300 Tg y^{-1} for loss [*Bey et al.*, 2001; *Mickley et al.*, 1999; comparison within *Hauglustaine et al.*, 1998]. The ozone production and loss rates calculated are within 10% of those found by *Bey et al.* [2001]. Our stratospheric input value (343 Tg y^{-1}) is below the range of recent studies (390-846 Tg y^{-1}) [*Bey et al.*, 2001; *Mickley et al.*, 1999; comparison within *Hauglustaine et al.*, 1998]. This value is also just below the range of 475 ± 120 Tg y^{-1} recently calculated by *McLinden et al.* [2000] based on measurements and tracer-

tracer correlations.

We also present in Table 3 the budgets of ozone in several geographical subdomains within MOZART-2, including the Northern and Southern Hemisphere, the tropics, and the northern and southern extratropics. We find a large hemispheric asymmetry in ozone production, with 53% more ozone being produced in the Northern Hemisphere. This asymmetry is even more pronounced if we consider only the extratropics, where the ozone production in the North is a factor of 4 larger than that in the South, reflecting the large difference in NO_x emissions in the two regions. We also find that more than half (54%) of the total stratosphere-troposphere exchange of ozone takes place in the northern extratropics, with the balance occurring in the tropics (32%) and the southern extratropics (14%). These values are sensitive to the definitions used for the regions in the budget analysis. If, instead of the current definition, we chose to define the tropics as extending from 25°S-25°N, and the tropopause height as approximately 150 hPa in the tropics and 250hPa in the extratropics, the total stratosphere-troposphere exchange would increase to 495 Tg y^{-1}, partitioned as 66% in the northern extratropics, 0% in the tropics, and 34% in the southern extratropics.

The vertical distribution of the chemical production and loss of ozone within the troposphere is shown in Table 4. The tropics are responsible for 75% of the total ozone production and loss, driven by large fluxes of UV radiation, high water vapor concentrations and temperatures, and biomass burning emissions and lightning. Within the tropics, production and loss are most rapid in the lower troposphere, accounting for 31% and 38%, respectively of the global totals. The tropical middle troposphere is also a major contributor to production (25%) and loss (31%). In the tropical upper troposphere, *gross* produc-

tion and loss rates are much slower, but there is a large *net* production of ozone (714 Tg/y) unlike the lower and middle troposphere in the tropics, where there is a net loss of ozone. Outside of the tropics, the most active ozone chemistry is found in the northern hemisphere lower troposphere. In this region, fueled by large anthropogenic NO_x emissions, 13% of the global production of tropospheric ozone occurs. There is also a significant net production of ozone (240 Tg/y) in this region. Ozone chemistry becomes slower with increasing altitude in the northern extratropics. Ozone production and loss rates are smallest in the southern extratropics, with a small net loss occurring in both the lower and middle troposphere. Globally, the most rapid chemistry occurs in the lower troposphere, accounting for 46% of the gross ozone production and 50% of the loss in the troposphere. The upper troposphere has the strongest *net* production of ozone, while the middle troposphere is a region of net loss and the lower troposphere is nearly in balance, with a small net production. We have also analyzed the continental-scale budgets from MOZART-2 for ozone and its precursors over Asia, the United States and Europe; these budgets will be presented in a future paper by *Mauzerall et al.* [2002].

5. Conclusions

We have presented a new global chemical transport model for the troposphere, MOZART, version 2. The model, which includes 63 chemical species and 167 chemical and photochemical reactions, simulates the global distributions of ozone and its precursors, including nitrogen oxides (NO_x), carbon monoxide (CO), and non-methane hydrocarbons (NMHCs). The model is an extension of version 1 of MOZART, and is built on the framework of the NCAR MATCH transport model. It can be driven with a variety of meteorological inputs. The version of MOZART-2 discussed in this paper uses meteorol-

ogy from the middle atmosphere version of the NCAR Community Climate Model (MACCM3), and runs with a horizontal resolution of 2.8° latitude x 2.8° longitude with 34 hybrid vertical levels extending up to 4 hPa (approximately 40 km). The model can also be driven with assimilated meteorological fields, such as those provided by NCEP or ECMWF. Surface emissions in the model are based on up-to-date emission inventories, and include sources from fossil fuel combustion, biofuel and biomass burning, biogenic and soil emissions, and oceanic emissions.

The model is evaluated by thoroughly comparing simulation results with observations from ozonesondes, aircraft, and surface monitoring stations. It successfully simulates the observed concentrations and seasonal cycle of ozone at most locations in the lower to middle troposphere. The agreement with observations of ozone is substantially improved compared with MOZART-1 [*Hauglustaine et al.*, 1998], in which tropospheric ozone was systematically too low, particularly at high latitudes and high altitudes. This improvement results from an improvement in the advection scheme, stronger convective transport to the upper troposphere, and improved chemical mechanism and emissions. There are still some disagreements between simulated ozone and observations. In the upper troposphere, at middle to high northern latitudes, the model tends to overestimate ozone in the vicinity of the tropopause by 25% or more at several sites. This may result from excessive downward transport of ozone from the stratosphere at these latitudes, as well as inadequate resolution of the tropopause location.

The calculated photochemical production and loss rates of ozone in the troposphere are on the high end of recent model studies, and are ~30-85% higher than the values calculated in MOZART-1 [*Hauglustaine et al.*, 1998; *Hauglustaine and Brasseur*,

2002]. The ozone production rate (~5250 Tg/y) and loss rate (~4750 Tg/y) dominate over the net stratospheric input rate (~350 Tg/y) and the loss by dry deposition (~850 Tg/y). The chemical sources and sinks of ozone in the troposphere are dominated by the tropics, where 75% of the production and loss occurs. Production and loss rates of ozone are roughly 50% higher in the northern hemisphere than the southern hemisphere, with an even larger asymmetry in the extratropics. Net production of ozone within the troposphere occurs primarily in the tropical upper troposphere and the northern extratropical lower troposphere. Other regions are either roughly in photochemical balance, or have a net loss of ozone. There is a strong hemispheric asymmetry in stratosphere-troposphere exchange of ozone; over half of the net influx of ozone occurs in the northern extratropics, a factor of 4 larger than occurs in the corresponding region of the southern hemisphere.

The reactive nitrogen species are crucial for regulating the production of ozone, and for controlling the abundance of the OH radical. The model simulates nitrogen oxides (NO_x) very well at almost all locations, over a range of concentrations spanning several orders of magnitude. The vertical profiles of PAN simulated by the model typically have a maximum in the middle to upper troposphere, in agreement with observations. However, the model tends to overestimate the magnitude of this peak in several regions in the tropics and subtropics, possibly due to excessive convective transport of PAN precursors combined with NO_x from lightning. Model concentrations and wet deposition fluxes of HNO_3 are in good agreement with observations. Concentrations of HNO_3 are not systematically biased high, as is the case for many recent global chemical transport model studies. HNO_3 concentrations are highly sensitive to the parameterization of wet deposition in the model.

Simulations of carbon monoxide are in good agreement with surface and airborne

observations, especially at tropical locations. At some high latitude stations, the model overestimates CO concentrations, possibly because of overestimates of biomass burning at high northern latitudes, or because of regional or seasonal errors in simulated OH concentrations. The non-methane hydrocarbons, ethane and propane, agree with observations to within ±25% at most locations. Oxygenated intermediate species, including carbonyls and peroxides, are useful tests of photochemical activity in the model. Carbonyl species, formaldehyde and acetone, are also simulated well by the model, although acetone is underestimated in some remote tropical regions, even with the addition of an oceanic source. The concentrations and vertical profiles of the hydroperoxides, hydrogen peroxide and methylhydroperoxide, agree well with observations in most regions.

The concentration of OH, which determines the removal rate of many reduced species from the troposphere, in MOZART-2 agrees well with the recent estimates of the global OH distribution by *Spivakovsky et al.* [2000] and of the lifetime of methane by IPCC [*Prather et al.*, 2001]. The OH abundance is sensitive to assumptions in the wet deposition scheme used in MOZART, as well as to the water vapor distribution and photolysis rates.

MOZART-2 provides a good overall simulation of the distributions of key species in tropospheric chemistry, including ozone and its key precursors. Future versions of the model will address several remaining problems in the simulation, including the overestimate of PAN in some regions of the upper troposphere. MOZART-2 has been developed to be a community model, and will be made available for download from the Atmospheric Chemistry Division at NCAR (http://acd.ucar.edu/models/MOZART/), along with the necessary input data files and documentation.

Acknowledgements. We thank our colleagues D. Hauglustaine, D. Kinnison, J.-F. Müller, and F. Sazzi for their help throughout the process of developing and evaluating of the model. In addition, we would like to thank D. Rotman, P. Cameron-Smith, and others at LNLL for useful discussions about the model, and for providing us with the code for their pressure fixer. This work also benefited from discussions with and assistance in evaluating the model from M. Newchurch, and D. Wuebbles and his group at UIUC.The work of D. Mauzerall was supported by NASA-ACMAP grant #NAG5-9810. The National Center for Atmospheric Research is operated by the University Corporation for Atmospheric Research under sponsorship of the National Science Foundation.

References

Andreae, M.O. and P. Merlet, Emission of trace gases and aerosols from biomass burning, *Global Biogeochem. Cycles*, in press, 2001.

Bey, I., D.J. Jacob, R.M. Yantosca, J.A. Logan, B.D. Field, A.M. Fiore, Q. Li, H.Y. Liu, L.J. Mickley, and M.G. Schultz, Global modeling of tropospheric chemistry with assimilated meteorology: Model description and evaluation, *J. Geophys. Res.*, *106*, 23,073-23,095, 2001.

Brasseur, G.P., D.A. Hauglustaine, S. Walters, P.J. Rasch, J.-F. Müller, C. Granier, and X.X. Tie, MOZART, a global chemical transport model for ozone and related chemical tracers, 1, Model description, *J. Geophys. Res.*, *103*, 28,265-28,289, 1998.

Brasseur, G.P., X.X. Tie, P.J. Rasch, and F. Lefèvre, A three-dimensional simulation of the Antarctic ozone hole: Impact of anthropogenic chlorine on the lower stratosphere and upper troposphere, *J. Geophys. Res.*, *102*, 8909-8930, 1997.

Brocheton, F., "Representation des emissions anthropiques dans les modeles de chimie-transport: Sensibilite a la representation spatiale des emissions et au degre de raffinement du schema chimique," PhD Thesis, Universite Paris 12 - Val de Marne, 1999.

DeFries, R.S., and J.R.G. Townshend, NDVI-derived land cover classification at global scales, *Int. J. Remote Sensing*, *15*, 3567-3586, 1994.

DeMore, W.B., S.P. Sander, D.M. Golden, R.F. Hampson, M.J. Kurylo, C.J. Howard, A.R. Ravishankara, C.E. Kolb, and M.J. Molina, Chemical kinetics and photochemical data for use in stratospheric modeling, *JPL Publication 97-4*, Jet Propulsion Laboratory, California Institute of Technology, Pasadena, CA, 1997.

Dentener, F.J., and P.J. Crutzen, A three-dimensional model of the global ammonia cycle, *J. Atmos. Chem.*, *19*, 331-369, 1994.

Emmons, L.K., D.A. Hauglustaine, J.-F. Müller, M.A. Carroll, G.P. Brasseur, D. Brunner, J. Staehelin, V. Thouret, and A. Marenco, Data composites of airborne observations of tropospheric ozone and its precursors, *J. Geophys. Res.*, *105*, 20,497-20,538, 2000.

Emmons, L., P. Hess, A. Klonecki, X. Tie, L. Horowitz, J.-F. Lamarque, D. Kinnison, G. Brasseur, E. Atlas,

E. Browell, C. Cantrell, F. Eisele, R.L. Mauldin, J. Merrill, B. Ridley, and R. Shetter, The budget of tropospheric ozone during TOPSE from two CTMs, submitted to *J. Geophys. Res., TOPSE special section*, 2002.

Friedl, R. (Ed.), Atmospheric effects of subsonic aircraft: Interim assessment report of the advanced subsonic technology program, *NASA Ref. Publ. 1400*, 143 pp., 1997.

Giorgi, F., and W.L. Chameides, The rainout parameterization in a photochemical model, *J. Geophys. Res., 90*, 7872-7880, 1985.

Granier, C., J.F. Müller, and G. Brasseur, The impact of biomass burning on the global budget of ozone and ozone precursors, *Proceedings ofthe Wengen Conference on Global Change Research: Biomass Burning and its Inter-Relationships with the Climate System*, in press, 1999.

Guenther, A., C. Geron, T. Pierce, B. Lamb, P. Harley, and R. Fall, Natural emissions of non-methane volatile organic compounds, carbon monoxide, and oxides of nitrogen from North America, *Atmos. Environ., 34*, 2205-2230, 2000.

Guenther, A., C.N. Hewitt, D. Erickson, R. Fall, C. Geron, T. Greadel, P. Harley, L. Klinger, M. Lerdau, W. McKay, T. Pierce, B. Scholes, R. Steinbrecher, R. Tallamraju, J. Taylor, and P. Zimmerman, A global model of natural volatile organic compound emissions, *J. Geophys. Res., 100*, 8873, 1995.

Hack, J.J., Parameterization of moist convection in the NCAR community climate model (CCM2), *J. Geophys. Res., 99*, 5551-5568, 1994.

Hansen, J., M. Sato, and R. Ruedy, Radiative forcing and climate response, *J. Geophys. Res., 102*, 6831-6864, 1997.

Hao, W.M., and M.-H. Liu, Spatial and temporal distribution of tropical biomass burning, *Glob. biogeochem. cycles, 8*, 495-503, 1994.

Hao, W.M., D.E. Ward, G. Olbu, and S.P. Baker, Emissions of CO_2, CO, and hydrocarbons from fires in diverse African savannah ecosystems, *J. Geophys. Res., 101*, 23,577-23,584, 1996.

Hauglustaine, D.A., and G.P. Brasseur, Evolution of tropospheric ozone under anthropogenic activities and associated radiative forcing of climate, *J. Geophys. Res., 106*, 32,337-32,360, 2001.

Hauglustaine, D.A., G.P. Brasseur, S. Walters, P.J. Rasch, J.-F. Müller, L.K. Emmons, and M.A. Carroll,

MOZART, a global chemical transport model for ozone and related chemical tracers, 2, Model results and evaluation, *J. Geophys. Res.*, *103*, 28,291-28,335, 1998.

Hess, P.G., S. Flocke, J.-F. Lamarque, M.C. Barth, and S. Madronich, Episodic modeling of the chemical structure of the troposphere as revealed duing the spring MLOPEX 2 intensive, *J. Geophys. Res.*, *105*, 26,809-26,839, 2000.

Holloway, T., H. Levy II, and P. Kasibhatla, Global distribution of carbon monoxide, *J. Geophys. Res.*, *105*, 12,123-12,147, 2000.

Holtslag, A., and B. Boville, Local versus nonlocal boundary-layer diffusion in a global climate model, *J. Clim.*, *6*, 1825-1842, 1993.

Horowitz, L.W., J. Liang, G.M. Gardner, and D.J. Jacob, Export of reactive nitrogen from North America during summertime: Sensitivity to hydrocarbon chemistry, *J. Geophys. Res.*, *103*, 13,451-13,476, 1998.

Jacob, D.J., B.D. Field, E. Jin, I. Bey, Q. Li, J.A. Logan, R.M. Yantosca and H.B. Singh, Atmospheric budget of acetone, *J. Geophys. Res.*, *107*(D10), 10.1029/2001JD000694, 2002.

Jaeglé, L., D.J. Jacob, W.H. Brune, and P.O. Wennberg, Chemistry of HOx radicals in the upper troposphere, *Atmos. Environ.*, *35*, 469-489, 2001.

Jöckel, P., R. von Kuhlmann, M.G. Lawrence, B. Steil, C.A.M. Brenninkmeijer, P.J. Crutzen, P.J. Rasch, and B. Eaton, On a fundamental problem in implementing flux-form advection schemes for tracer transport in 3-dimensional general circulation and chemical tracer models, *Q.J.R. Meteorol. Soc.*, in press, 2001.

Kiehl, J.T., J.J. Hack, G.B. Bonan, B.A. Boville, D.L. Williamson, and P.J. Rasch, The National Center for Atmospheric Research Community Climate Model: CCM3, *J. Climate*, *11*, 1131-1149, 1998.

Klinger, L.F., Greenberg, J., Guenther, A., Tyndall, G., Zimmerman, P., M'Bangui, M., Moutsamboté, J.-M., Kenfack, D., Patterns in volatile organic compound emissions along a savanna-rainforest gradient in central Africa, *J. Geophys. Res.*, *103*, 1443-1454, 1998.

Lawrence, M.G., P.J. Crutzen, P.J. Rasch, B.E. Eaton, and N.M. Mahowald, A model for studies of tropospheric photochemistry: Description, global distributions, and evaluation, *J. Geophys. Res.*, *104*,

26,245-26,277, 1999.

Lelieveld, J., and F.J. Dentener, What controls tropospheric ozone?, *J. Geophys. Res.*, *105*, 3531-3551, 2000.

Levy, H., II, W.J. Moxim, and P.S. Kasibhatla, A global three-dimensional time-dependent lightning source of tropospheric NO_x, *J. Geophys. Res.*, *101*, 22,911-22,922, 1996.

Levy, H., II, W.J. Moxim, A.A. Klonecki, and P.S. Kasibhatla, Simulated tropospheric NO_x: Its evaluation, global distribution and individual source contributions, *J. Geophys. Res.*, *104*, 26,279-26,306, 1999.

Lin, S.-J., and R.B. Rood, Multidimensional flux-form semi-lagrangian transport schemes, *Mon. Wea. Rev.*, *124*, 2046-2070, 1996.

Logan, J.A., M.J. Prather, S.C. Wofsy, and M.B. McElroy, *Tropospheric chemistry: a global perspective, J. Geophys. Res.*, *86*, 7210-7254, 1981.

Logan, J.A., An analysis of ozonesonde data for the troposphere: Recommendations for testing 3-D models and development of a gridded climatology for tropospheric ozone, *J. Geophys. Res.*, *104*, 16,115-16,149, 1999.

Madronich, S. and S. Flocke, The role of solar radiation in atmospheric chemistry, in Handbook of Environmental Chemistry (P. Boule, ed.), Springer-Verlag, Heidelberg, 1998, pp. 1-26.

Muazerall, D.L., L.W. Horowitz, and N. Kim, Factors regulating the seasonal cycle of inter-continental air pollution transport between Asia, the United States, and Europe, to be submitted to *J. Geophys. Res.*, 2002.

McLinden, C.A., S.C. Olsen, B. Hannegan, O. Wild, M.J. Prather, and J. Sundet, Stratospheric ozone in 3-D models: A simple chemistry and the cross-tropopause flux, *J. Geophys. Res.*, *105*, 14,653-14,665, 2000.

Mickley, L.J., P.P. Murti, D.J. Jacob, J.A. Logan, D. Rind, and D. Koch, Radiative forcing from tropospheric ozone calculated with a unified chemistry-climate model, *J. Geophys. Res.*, *104*, 30,153-30,172, 1999.

Moxim, W.J., H. Levy II, A model analysis of the tropical South Atlantic Ocean tropospheric ozone maximum: The interaction of transport and chemistry, *J. Geophys. Res.*, *105*, 17,393-17,415, 2000.

Müller, J.-F., Geographical distribution and seasonal variation of surface emissions and deposition velocities of atmospheric trace gases, *J. Geophys. Res.*, *97*, 3787-3804, 1992.

National Research Council (NRC), *Rethinking the Ozone Problem in Urban and Regional Air Pollution*, Nat. Acad. Press, Washington, D.C., 1991.

Novelli, P.C., K.A. Masarie, and P.M. Lang, Distributions and recent changes of carbon monoxide in the lower troposphere, *J. Geophys. Res.*, *103*, 19,015-19,033, 1998.

Olivier, J.G.J., A.F. Bouwman, C.W.M. van der Maas, J.J.M. Berdowski, C. Veldt, J.P.J. Bloos, A.J.H. Visschedijk, P.Y.J. Zandveld, and J.L. Haverlag, Description of EDGAR version 2.0: A set of global emission inventories of greenhouse gases and ozone-depleting substances for all anthropogenic and most natural sources on a per country basis and on a 1x1 degree grid, *RIVM report 771060 002/ TNO-MEP report R96/119*, National Institute of Public Health and the Environment, Bilthoven, the Netherlands, 1996.

Orlando, J.J., G.S. Tyndall, and S.E. Paulson, Mechanism of the OH-initiated oxidation of methacrolein, *Geophys. Res. Lett.*, *26*, 2191-2194.

Pickering, K.E., Y. Wang, W.-K. Tao, C. Price, and J.-F. Müller, Vertical distributions of lightning NO_x for use in regional and global chemical transport models, *J. Geophys. Res.*, *103*, 31,203-31,216, 1998.

Prather, M.J., and D.J. Jacob, A persistent imbalance in HO_x and NO_x photochemistry of the upper troposphere driven by deep tropical convection, *Geophys. Res. Lett.*, *24*, 3189-3192, 1997.

Prather, M., D. Ehhalt, F. Dentener, R. Derwent, E. Dlugokencky, E. Holland, I. Isaksen, J. Katima, V. Kirchhoff, P. Matson, P. Midgley, M. Wang, Atmospheric Chemistry and Greenhouse Gases, In: *Climate Change 2001: The Scientific Basis. Contribution of Working Group I to the Third Assessment Report of the Intergovernmental Panel on Climate Change* [Houghton, J.T., Y. Ding, D.J. Griggs, M. Noguer, P.J. van der Linden, X. Dai, K. Maskell, and C.A. Johnson (eds.)]. Cambridge University Press, Cambridge, United Kingdom and New York, NY, USA, 881pp., 2001.

Price, C., J. Penner, and M. Prather, NO_x from lightning, 1, Global distribution based on lightning physics, *J. Geophys. Res.*, *102*, 5929-5941, 1997.

Randel, W.J., F. Wu., J.M. Russell III, A. Roche and J. Waters, Seasonal cycles and QBO variations in strato-

spheric CH_4 andH_2O observed in UARS HALOE data. *J. Atmos. Sci.*, *55*, 163-185, 1998.

Rasch, P.J., N.M. Mahowald, and B.E. Eaton, Representations of transport, convection, and the hydrologic cycle in chemical transport models: Implications for the modeling of short-lived and soluble species, *J. Geophys. Res.*, *102*, 28,127-28,138, 1997.

Sander, S.P., R.R. Friedl, W.B. DeMore, D.M. Golden, M.J. Kurylo, R.F. Hampson, R.E. Huie, G.K. Moortgat, A.R. Ravishankara, C.E. Kolb, and M.J. Molina, *Chemical kinetics and photochemical data for use in stratospheric modeling, Supplement to Evalulation 12: Update of key reactions, JPL Publ. 00-3*, Jet Propul. Lab., Pasadena, Calif., 2000.

Singh, H.B., Y. Chen, A.C. Staudt, D.J. Jacob, D.R. Blake, B.G. Heikes, and J. Snow, Evidence from the South Pacific troposphere for large global abundances and sources of oxygenated organic compounds, *Nature*, in press, 2001.

Spivakovsky, C.M., J.A. Logan, S.A. Montzka, Y.J. Balkanski, M. Foreman-Fowler, D.B.A. Jones, L.W. Horowitz, A.C. Fusco, C.A.M. Brenninkmeijer, M.J. Prather, S.C. Wofsy, and M.B. McElroy, Three-dimensional climatological distribution of tropospheric OH: Update and evaluation, *J. Geophys. Res.*, *105*, 8931-8980, 2000.

Thompson, A.M., and J. C. Witte, SHADOZ (Southern Hemisphere ADditional OZonesondes): A new data set for the Earth Science Community, *Earth Observer*, *11*, 27-30, 1999. Web site: http://code916.gsfc.nasa.gov/Data_services/shadoz/.

Tie, X., G. Brasseur, L. Emmons, L. Horowitz, and D. Kinnison, Effects of Aerosols on Tropospheric Oxidants: A Global Model Study, *J. Geophys. Res.*, *106*, 22,931-22,964, 2001.

Tie, X., L. Emmons, L. Horowitz, G. Brasseur, B. Ridley, E. Atlas, C. Stround, P. Hess, A. Klonecki, S. Madronich, R. Talbot, and J. Dibb, Effect of sulfate aerosol on tropospheric NO_x and ozone budgets: Model simulations and TOPSE evidence, submitted to *J. Geophys. Res., TOPSE special section*, 2002.

Wesely, M.L., Parameterization of surface resistance to gaseous dry deposition in regional-scale numerical models, *Atmos. Environ.*, *23*, 1293-1304, 1989.

Yienger, J.J., and H. Levy II, Empirical model of global soil-biogenic NO_x emissions, *J. Geophys. Res.*, *100*,

11,447-11,464, 1995.

Zhang, G.J., and N.A. McFarlane, Sensitivity of climate simulations to the parameterization of cumulus convection in the Canadian Climate Centre general circulation model, *Atmos. Ocean*, *33*, 407-446, 1995.

Zhou, X.L., and K. Mopper, Photochemical production of low-molecular-weight carbonyl compounds in seawater and surface microlayer and their air-sea exchange, *Mar. Chem.*, *56*, 201-213, 1997.

Figure 1. Monthly mean surface emissions (in units of 10^{10} molecules cm^{-2} s^{-1}) of nitrogen oxides (as NO) from industrial sources (top), biomass and biofuel burning (middle), and biogenic emissions from soil (bottom) for January (left) and July (right).

Figure 2. Monthly mean simulated concentrations of ozone (in ppbv) in January and July at hybrid model levels corresponding approximately to 970 hPa and 510 hPa.

Figure 3. Comparison of observed (dotted lines) and simulated (solid lines) seasonal vertical profiles of ozone volume mixing ratio (ppbv), and standard deviations (horizontal lines). Observations are from ozonesonde measurements compiled by Logan [1999]. Station names and locations (latitude and longitude) are given above each plot.

Figure 4. Monthly mean observed (dotted lines) and simulated (solid lines) ozone volume mixing ratios (ppbv), and standard deviations (vertical lines). Observations are from ozonesonde measurements compiled by Logan [1999].

Figure 5. Same as Figure 2, but for NO_x ($NO+NO_2$) (in pptv).

Figure 6. Mean observed (box-whisker) and simulated (solid and dahed lines) regional vertical profiles of NO_x (pptv). Observations are from aircraft field campaigns (see Table 2 for listing of field campaigns and regions), as compiled by *Emmons et al.* [2000]. The observed values are shown as mean (star), median (vertical bar), central 50% of the data (box), and central 90% of the data (horizontal line). The simulated values are shown as mean (solid line) $\pm 1\sigma$ standard deviation (dashed lines). Note that in some field campaigns the reported "observed" NO_x concentration is computed as the sum of the observed NO concentration and the NO_2 concentration calculated by a box model (see *Emmons et al.* [2000]).

Figure 7. Same as Figure 6 but for PAN (pptv).

Figure 8. Same as Figure 6 but for HNO_3 (pptv).

Figure 9. Comparison of observed and simulated annual wet deposition fluxes of HNO_3 (mmole m^{-2} y^{-1}). Observations are compiled by *Dentener and Crutzen* [1994], and are listed in Table V of that work. Plotting symbols are coded based on the location of the station: Europe (Θ), South America(+), North America (O), East Asia ($\times$), South Asia ($\square$), Oceania (Δ), Africa (∇), and other ($*$). The thick line is the 1:1 line, and the thin lines are the 1:2 and 2:1. The zero-intercept reduced major axis regression line has a slope of 1.25, with a correlation coefficient of r^2=0.81.

Figure 10. Same as Figure 2, but for CO (in ppbv).

Figure 11. Comparison of observed (dotted lines) and simulated (solid lines) monthly mean carbon monoxide volume mixing ratios (ppbv) at surface sites. Observations are from the NOAA/CMDL flask measurement network [*Novelli et al.*, 1998]. Station names and locations (latitude and longitude) are given above each plot. Vertical bars indicate the

standard deviations of the observations or model results within a month.

Figure 12. Same as Figure 6 but for CO (ppbv).

Figure 13. Same as Figure 6 but for ethane (pptv).

Figure 14. Same as Figure 6 but for formaldehyde (pptv).

Figure 15. Same as Figure 6 but for acetone (pptv).

Figure 16. Same as Figure 6 but for hydrogen peroxide (pptv).

Figure 17. Same as Figure 6 but for methlyhydroperoxide (pptv).

Figure 18. Zonally and monthly averaged concentrations of OH (in units of 10^5 molecules cm^{-3}) for January, April, July, and October.

Table 1: Surface Emissions in MOZART

Species	Industry / Fossil fuel	Biofuel combustion	Biomass burning	Biogenic / Soil	Oceans	Total
NO (TgN/y)	23.11	1.25	9.81	6.62	0	40.79
CO (Tg/y)	306.89	231.04	486.63	160.10	10.00	1195.05
C_2H_6 (TgC/y)	3.18	1.43	4.06	0.80	0.08	9.56
C_3H_8 (TgC/y)	5.02	0.47	1.10	1.64	0.11	8.33
C_2H_4 (TgC/y)	2.02	2.88	7.89	4.29	2.07	19.16
C_3H_6 (TgC/y)	0.86	1.42	2.81	0.86	2.52	8.46
C_4H_{10} (TgC/y)	11.08	4.99	7.55	0	6.26	29.88
CH_3COCH_3 (Tg/y)	1.00	0.11	2.51	19.95	13.45	37.02
ISOP (TgC/y)	0	0	0	410.39	0	410.39
$C_{10}H_{16}$ (TgC/y)	0	0	0	129.06	0	129.06
CH_2O (Tg/y)	0.63	0.53	5.81	0	0	6.97
CH_3OH (Tg/y)	0	9.73	15.56	286.73	0	312.02
CH_4 (Tg/y)[a]	94.97	14.01	71.84	145.69	9.98	489.47
N_2O (Tg/y)	5.00	0.16	1.72	20.73	11.31	38.92
H_2 (Tg/y)	14.86	3.37	16.03	3.00	3.00	40.26

a.The emissions for CH_4 also include 59.94 Tg/y from rice cultivation and 93.05 Tg/y from ruminants.

Table 2: Regions for Vertical Profiles of Aircraft Observations

Region name	Expedition	Latitude	Longitude	Date
North Pacific	PEM-West-A	15-35°N	180-150°W	Sep 16 - Oct 21, 1991
Japan Coast, East	PEM-West-A	25-40°N	135-150°E	Sep 16 - Oct 21, 1991
Phillipine Sea	PEM-West-A	5-20°N	135-150°E	Sep 16 - Oct 21, 1991
Japan coast, East	PEM-West-B	25-40°N	135-150°E	Feb 7 - Mar 14, 1994
Phillipine Sea	PEM-West-B	5-20°N	135-150°E	Feb 7 - Mar 14, 1994
Africa coast, West	TRACE-A	25-5°S	0-10°E	Sep 21 - Oct 26, 1992
South Atlantic	TRACE-A	20°S-Eq	20-10°W	Sep 21 - Oct 26, 1992
Brazil, East	TRACE-A	15-5°S	50-40°W	Sep 21 - Oct 26, 1992
Christmas Island	PEM-Tropics-A	Eq-10°N	160-140°W	Aug 15 - Oct 15, 1996
Tahiti	PEM-Tropics-A	20°S-Eq	160-130°W	Aug 15 - Oct 15, 1996
Fiji	PEM-Tropics-A	30-10°S	170°E-170°W	Aug 15 - Oct 15, 1996
Guayaquil	PEM-Tropics-A	15°S-10°N	95-75°W	Aug 15 - Sep 26, 1996
Christmas Island	PEM-Tropics-B	Eq-10°N	160-140°W	Mar 6 - Apr 18, 1999
Tahiti	PEM-Tropics-B	20°S-Eq	160-130°W	Mar 6 - Apr 18, 1999
Fiji	PEM-Tropics-B	30-10°S	170°E-170°W	Mar 6 - Apr 18, 1999
East Atlantic	SONEX	35-45°N	35-15°W	Oct 7 - Nov 12, 1997
Ireland	SONEX	50-60°N	15-5°W	Oct 7 - Nov 12, 1997

Table 3: Annual Mean Budget of Tropospheric Ozone in MOZART-2

	Source (Sink) [Tg O_3 / yr]					
Process	Global	Northern Hemisphere	Southern Hemisphere	Tropics	Northern Extratropics	Southern Extratropics
Influx from stratosphere[a]	343[b]	256	87	109	187	47
Photochemical production	5258	3178	2080	3951	1055	251
Photochemical loss	-4749	-2816	-1933	3569	-868	-311
Dry deposition	-857	-583	-274	-458	-319	-80
Net tropospheric transport	0	-40	40	-32	-60	92
Burden (Tg O_3)	362	203	159	203	99	60

For this budget, the tropics are defined to extend from 30°S-30°N, and the extratropics from 30-90°N or S. The tropopause is defined as the hybrid model level interface corresponding to approximately 100 hPa in the tropics and 250hPa in the extratropics.

a. Includes advection, convection and vertical diffusion.

b. This term consists of advection (334 Tg/y) and convection and vertical diffusion (9 Tg/y).

Table 4: Regional Production and Loss of Tropospheric Ozone in MOZART-2 [Tg O_3/yr]

Vertical region[a]	Production / Loss	Southern extratropics	Tropics	Northern extratropics	Total
Upper troposphere (400 hPa - tropopause)	P	52	1005	1005	1163
	L	45	291	100	436
Middle troposphere (700-400 hPa)	P	99	1292	261	1653
	L	143	1473	319	1936
Lower troposphere (surface - 700 hPa)	P	100	1654	689	2442
	L	123	1805	449	2377
Total (surface - tropopause)	P	251	3951	1055	5258
	L	311	3569	868	4749

For this budget, the definitions of the tropics, extratropics, and tropopause are as in Table 3.

a.The vertical regions used for this budget are defined to extend between the hybrid model level interfaces corresponding to the approximate pressures shown.

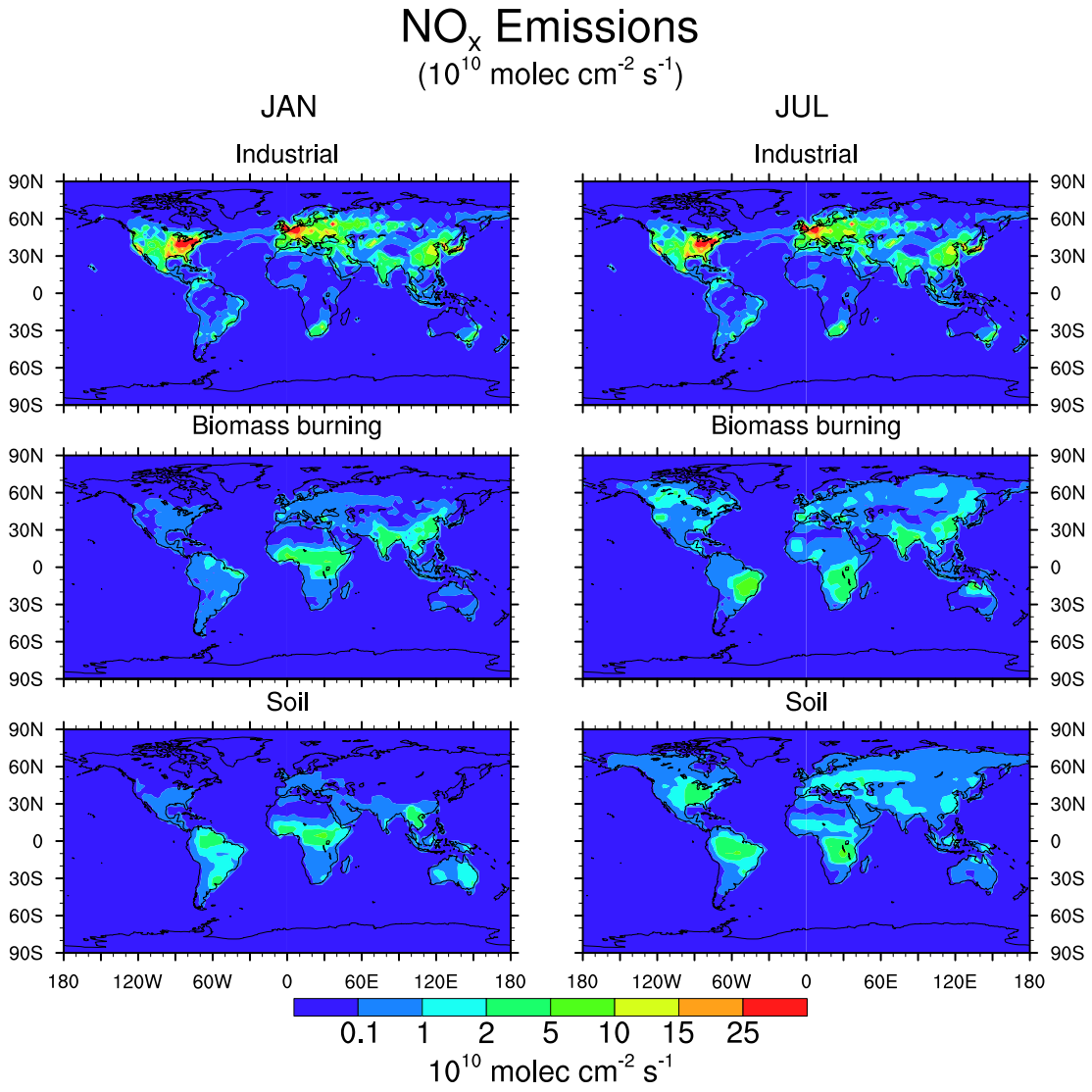

Figure 1. Monthly mean surface emissions (in units of 10^{10} molecules cm^{-2} s^{-1}) of nitrogen oxides (as NO) from industrial sources (top), biomass and biofuel burning (middle), and biogenic emissions from soil (bottom) for January (left) and July (right).

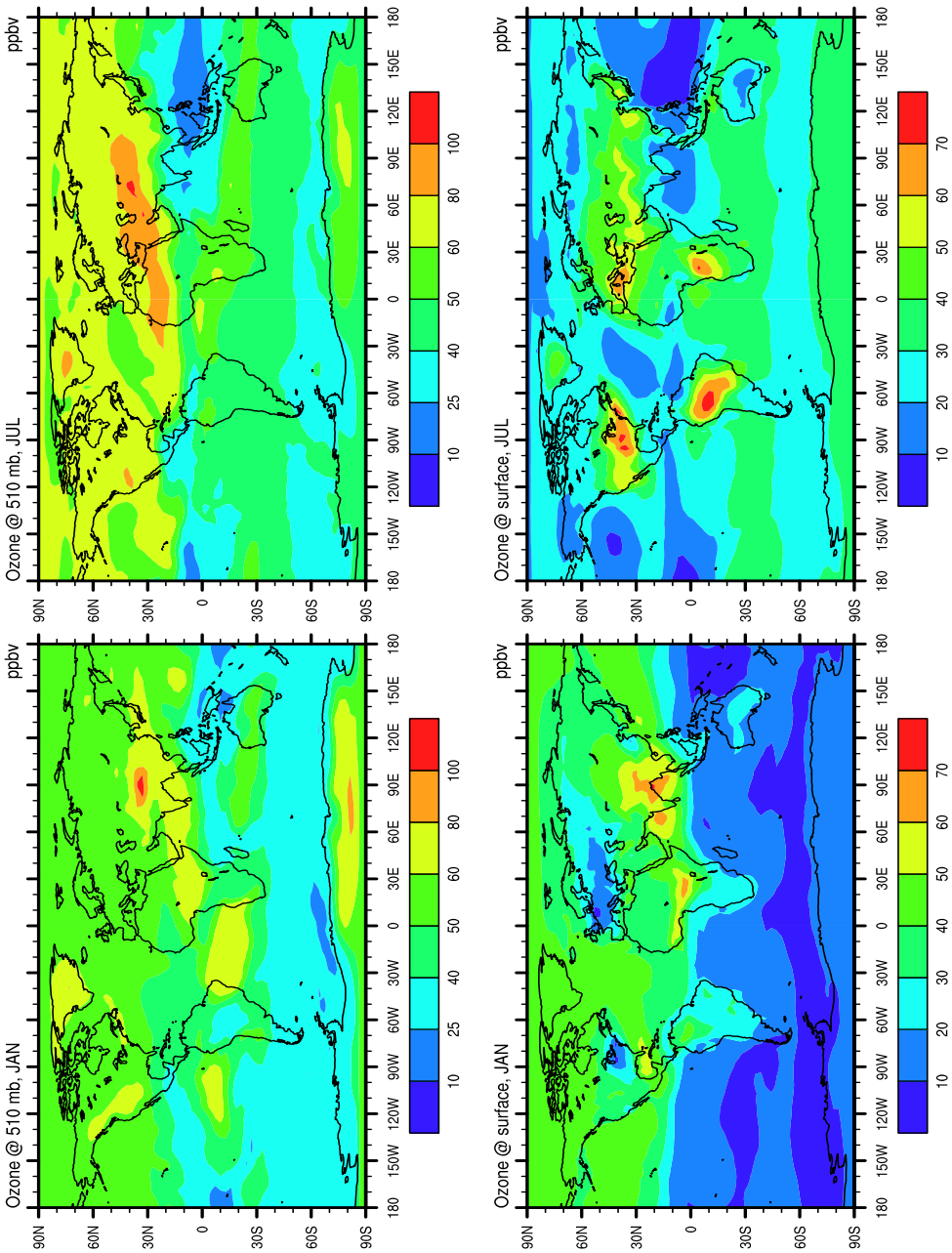

Figure 2. Monthly mean simulated concentrations of ozone (in ppbv) in January and July at hybrid model levels corresponding approximately to 970 hPa and 510 hPa.

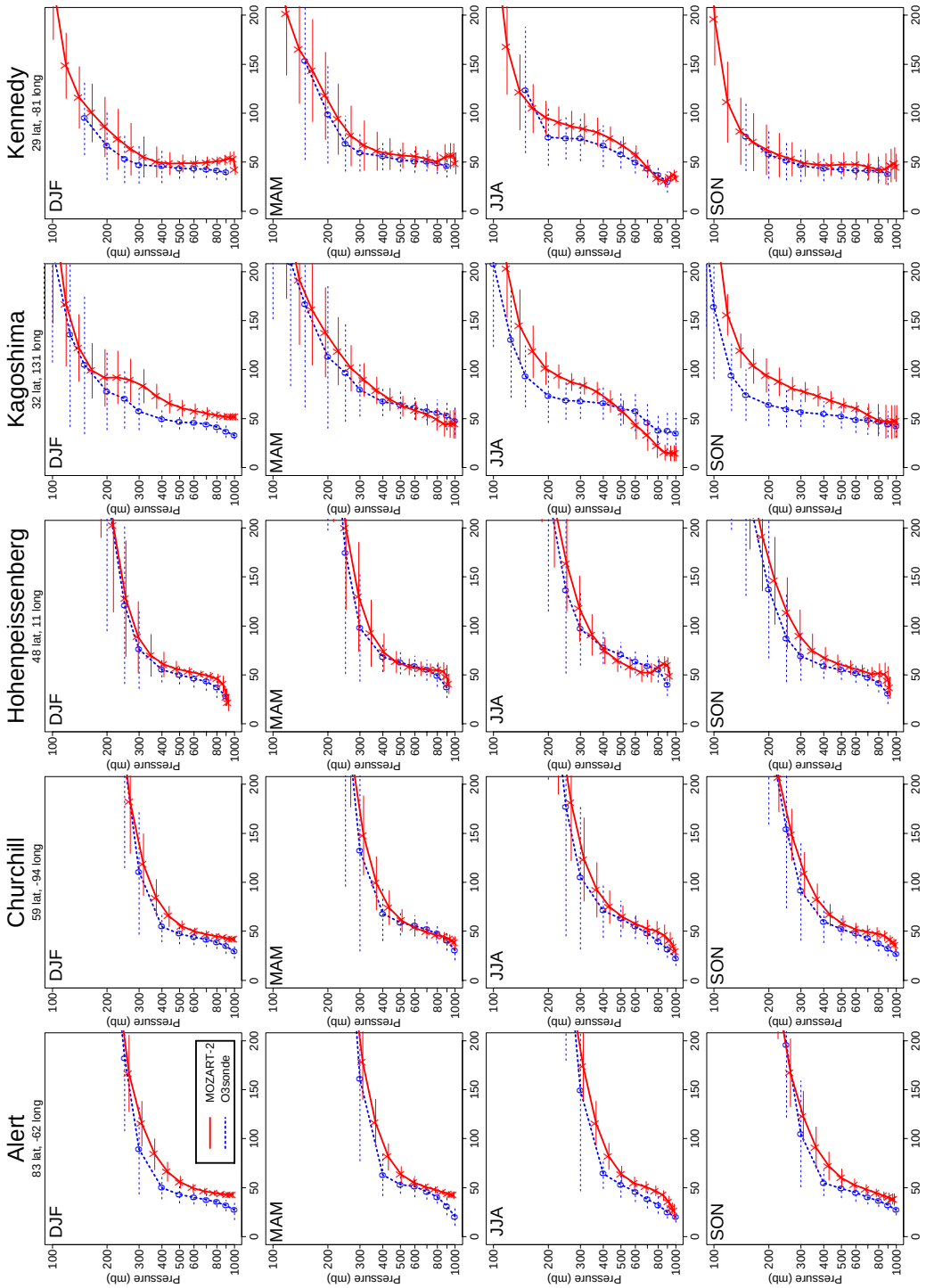

Figure 3. Comparison of observed (dotted lines) and simulated (solid lines) seasonal vertical profiles of ozone volume mixing ratio (ppbv), and standard deviations (horizontal lines). Observations are from ozonesonde measurements compiled by Logan [1999]. Station names and locations (latitude and longitude) are given above each plot.

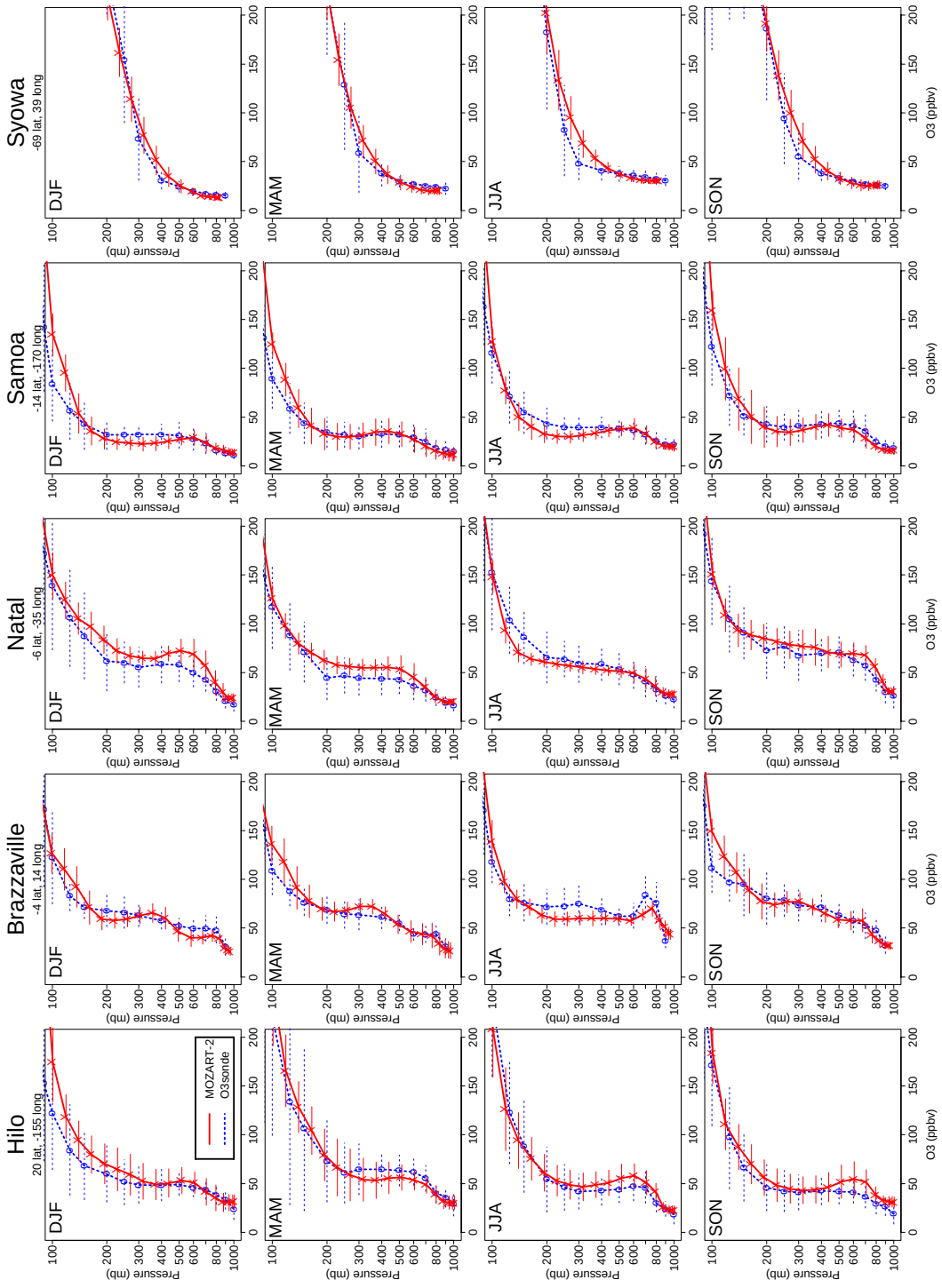

Figure 3 (cont'd).

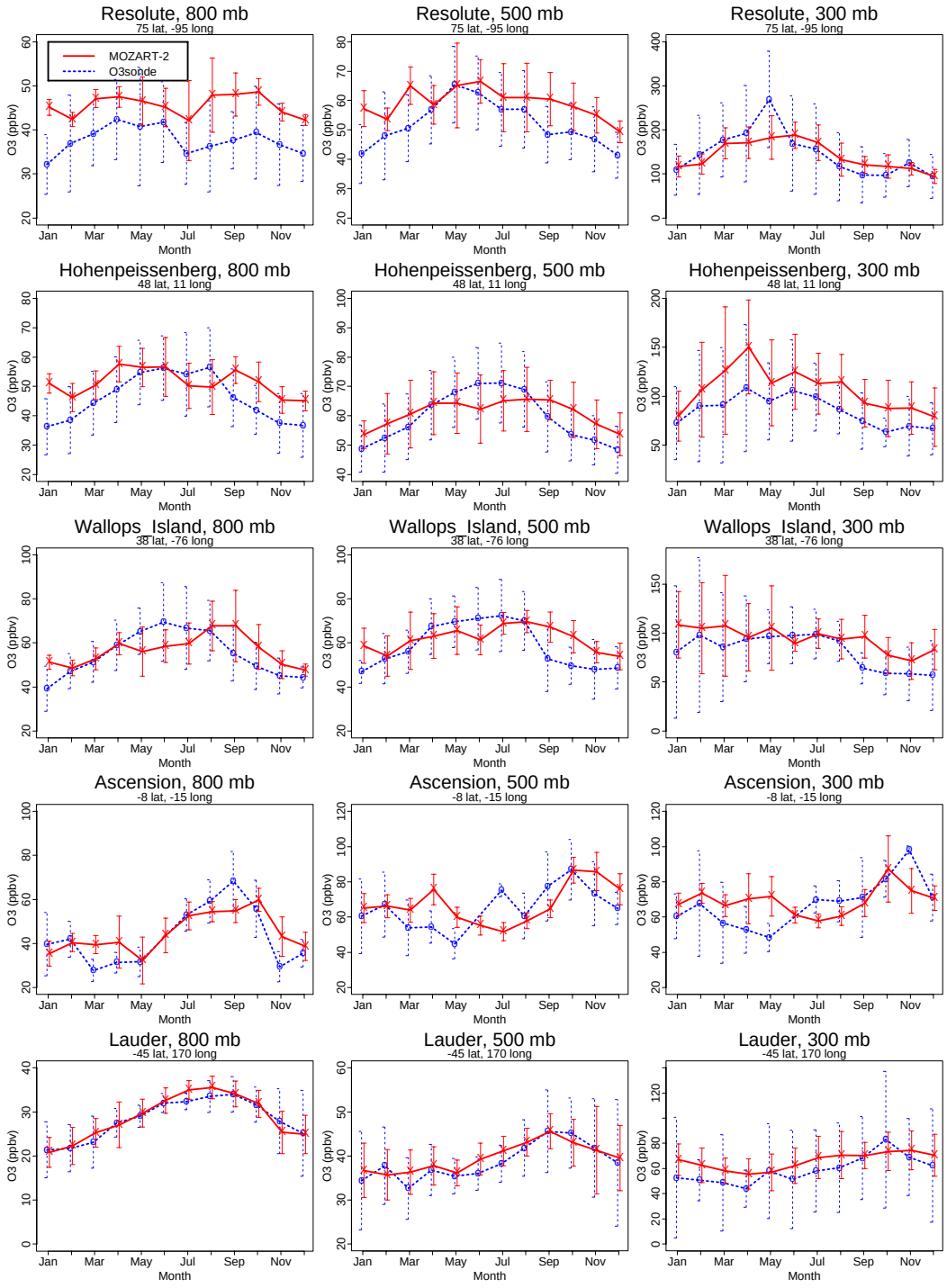

Figure 4. Monthly mean observed (dotted lines) and simulated (solid lines) ozone volume mixing ratios (ppbv), and standard deviations (vertical lines). Observations are from ozonesonde measurements compiled by Logan [1999].

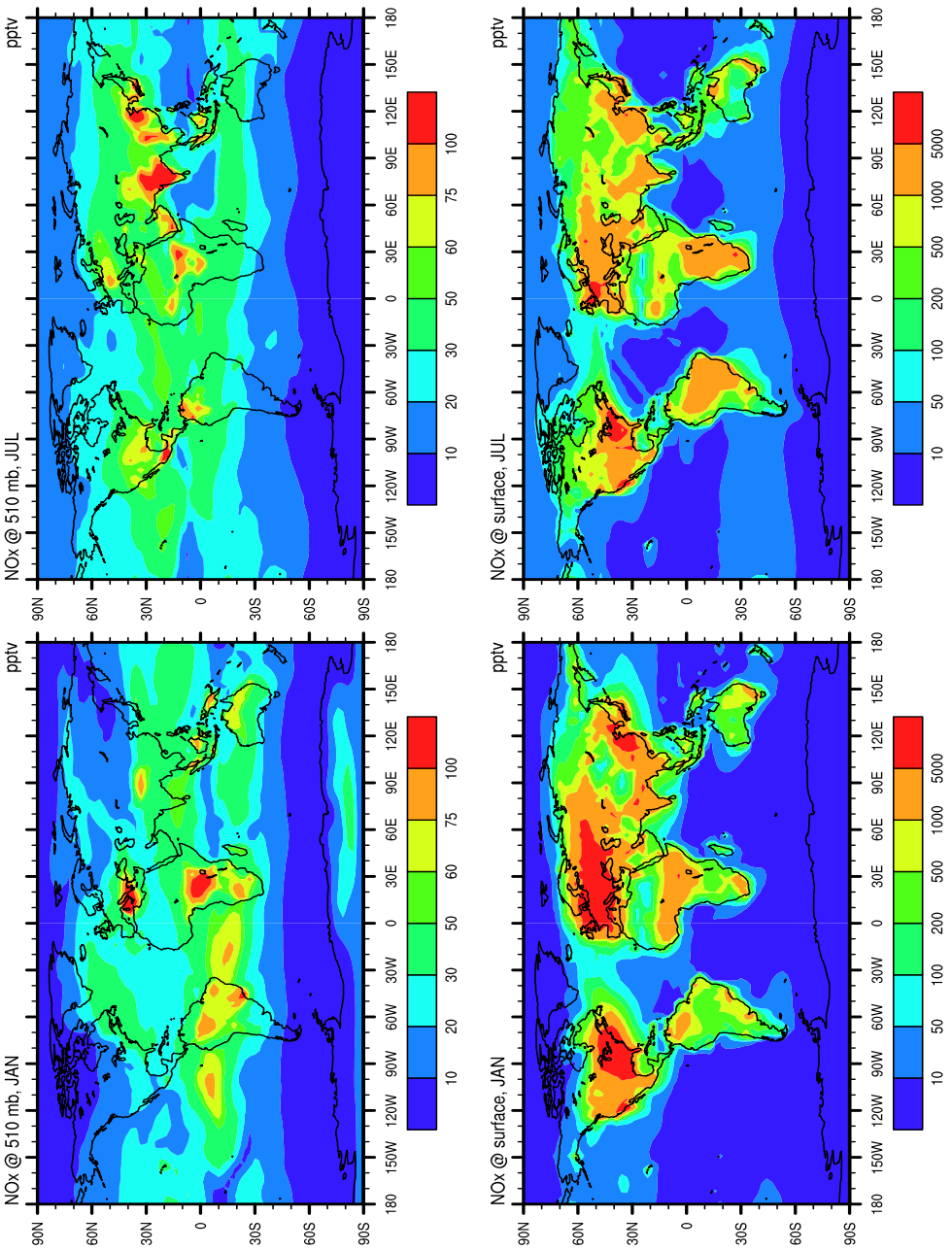

Figure 5. Same as Figure 2, but for NO_x ($NO+NO_2$) (in pptv).

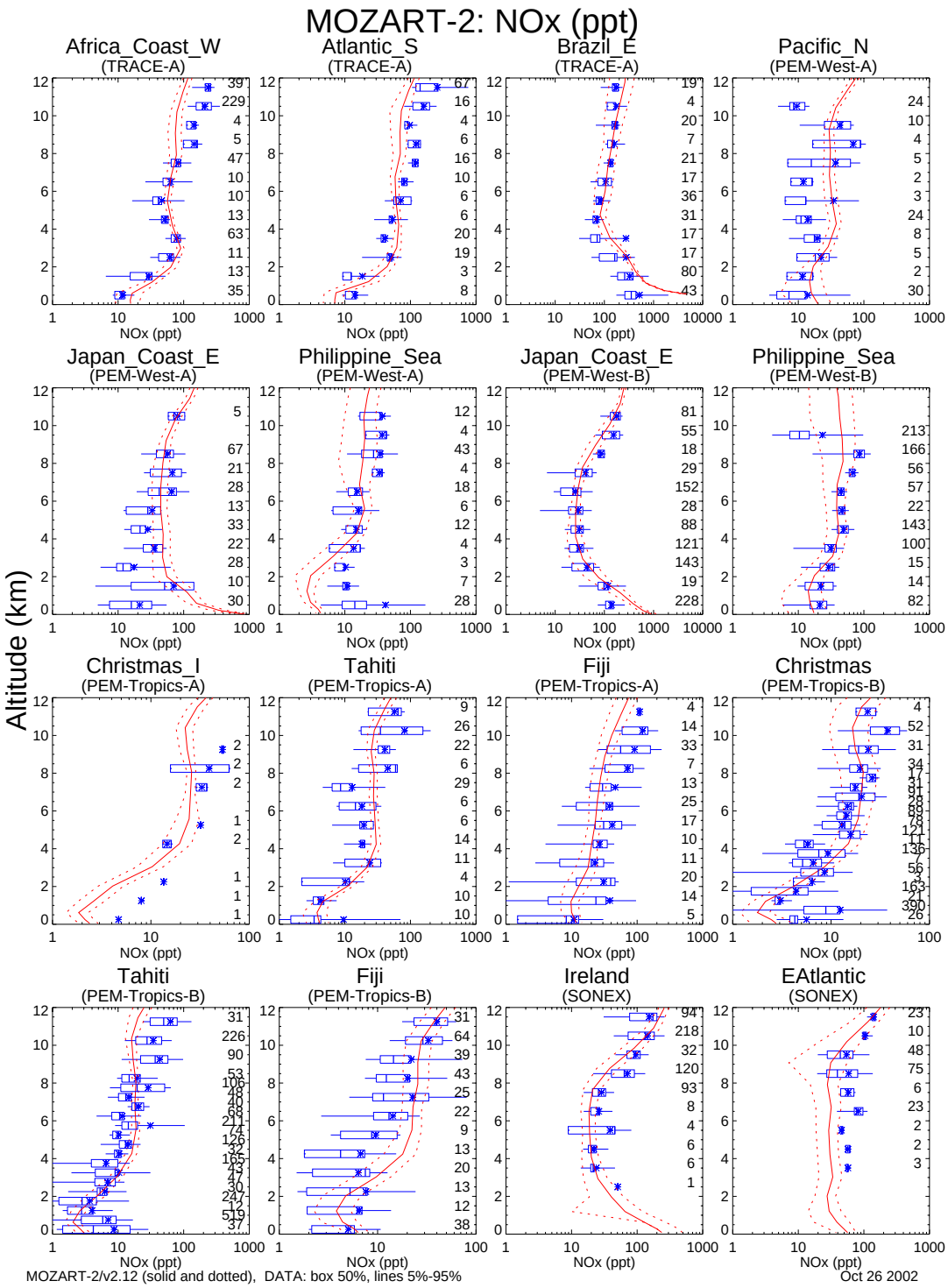

Figure 6. Mean observed (box-whisker) and simulated (solid and dahed lines) regional vertical profiles of NO_x (pptv). Observations are from aircraft field campaigns (see Table 2 for listing of field campaigns and regions), as compiled by *Emmons et al.* [2000]. The observed values are shown as mean (star), median (vertical bar), central 50% of the data (box), and central 90% of the data (horizontal line). The simulated values are shown as mean (solid line) $\pm 1\sigma$ standard deviation (dashed lines). Note that in some field campaigns

the reported "observed" NO_x concentration is computed as the sum of the observed NO concentration and the NO_2 concentration calculated by a box model (see *Emmons et al.* [2000]).

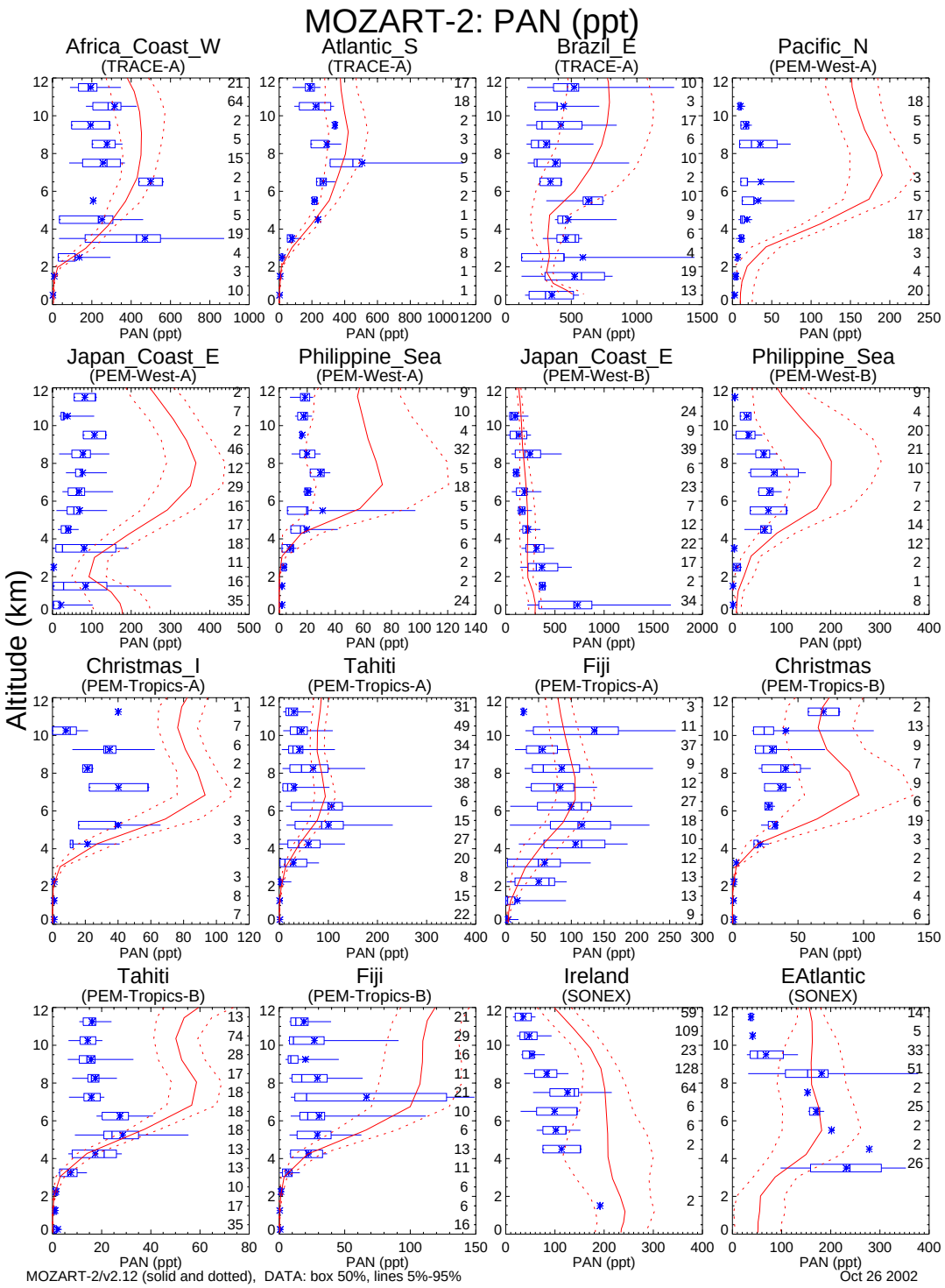

Figure 7. Same as Figure 6 but for PAN (pptv).

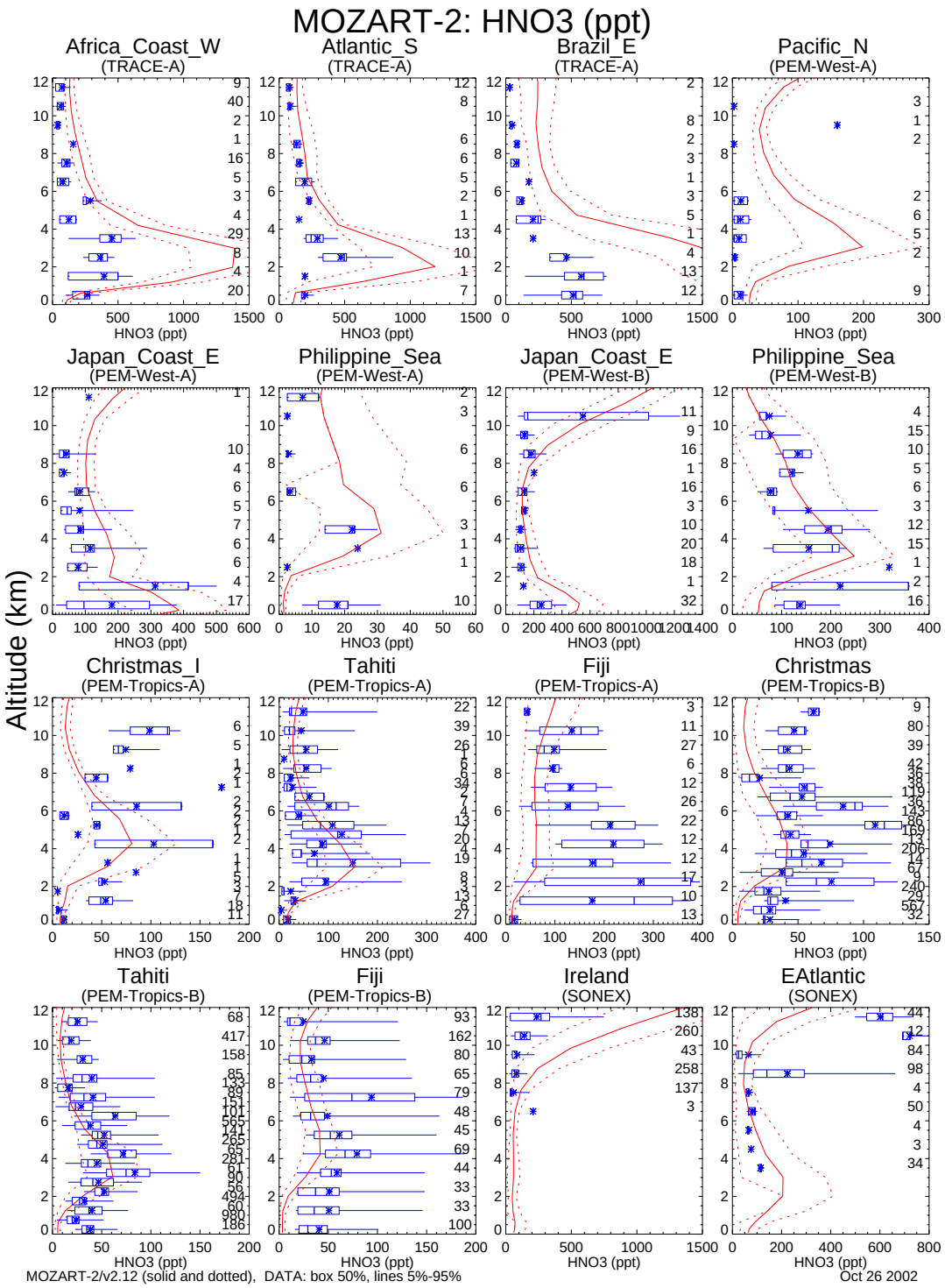

Figure 8. Same as Figure 6 but for HNO_3 (pptv).

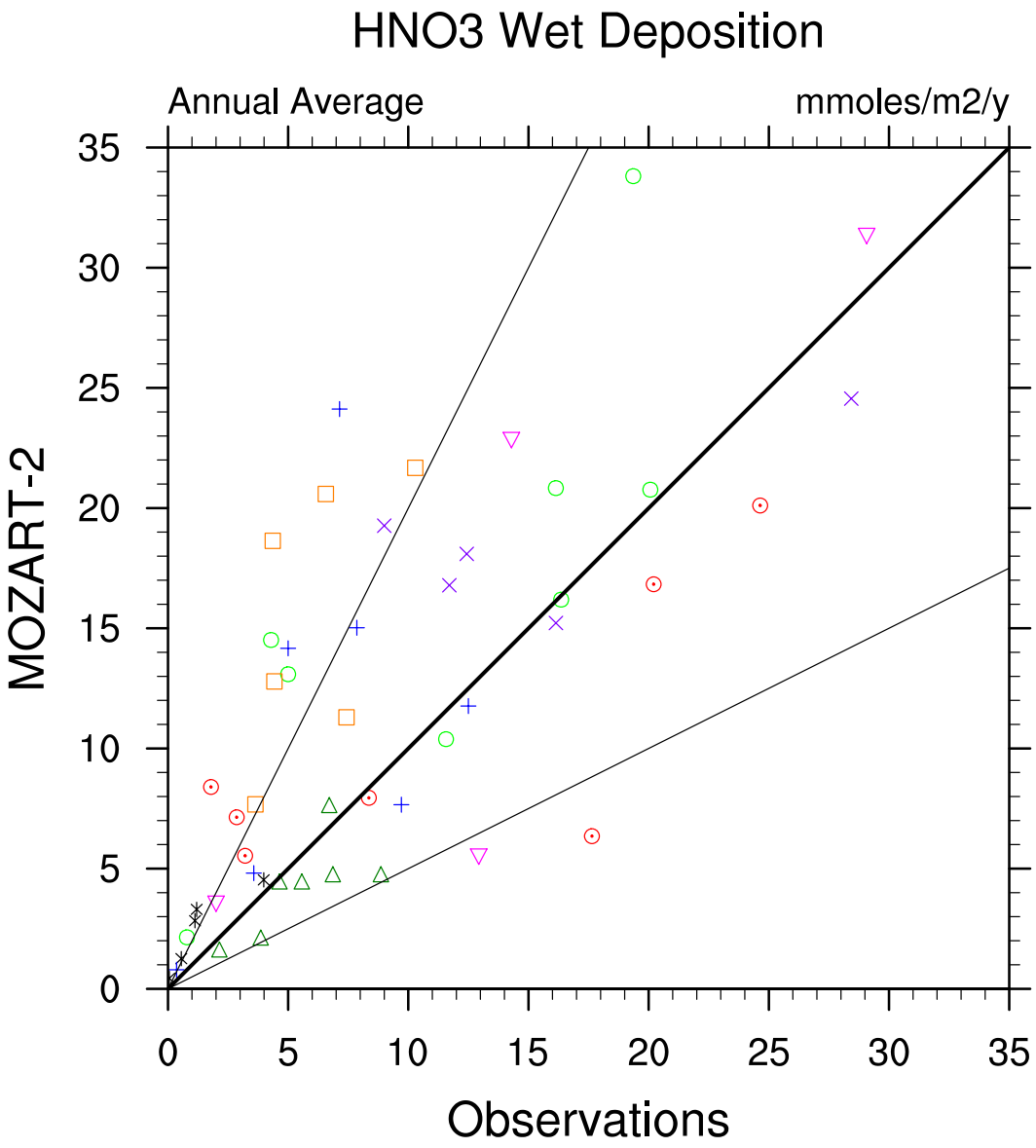

Figure 9. Comparison of observed and simulated annual wet deposition fluxes of HNO_3 (mmole m^{-2} y^{-1}). Observations are compiled by *Dentener and Crutzen* [1994], and are listed in Table V of that work. Plotting symbols are coded based on the location of the station: Europe (Θ), South America(+), North America (O), East Asia (×), South Asia (❑), Oceania (Δ), Africa (∇), and other (∗). The thick line is the 1:1 line, and the thin lines are the 1:2 and 2:1. The zero-intercept reduced major axis regression line has a slope of 1.25, with a correlation coefficient of r^2=0.81.

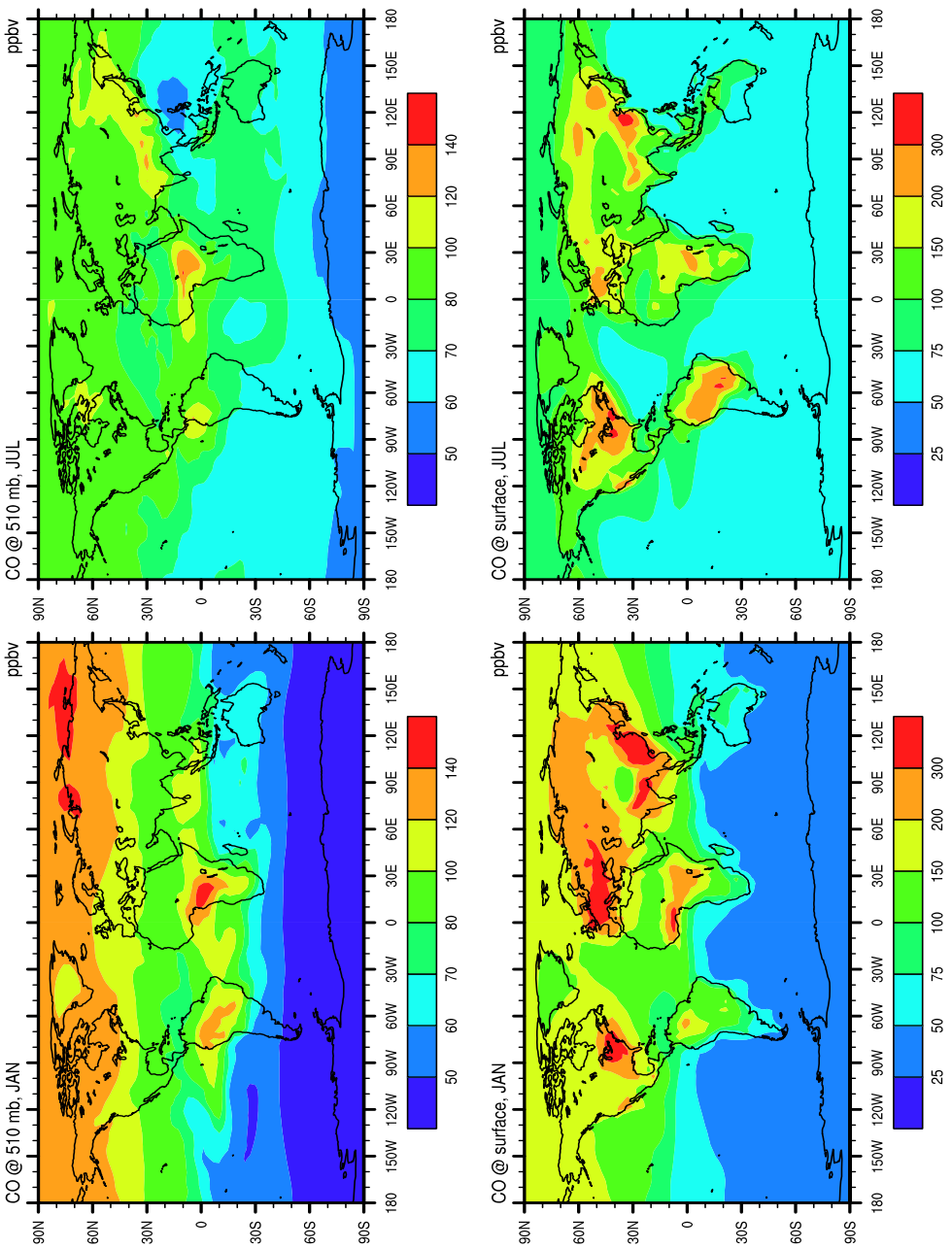

Figure 10. Same as Figure 2, but for CO (in ppbv).

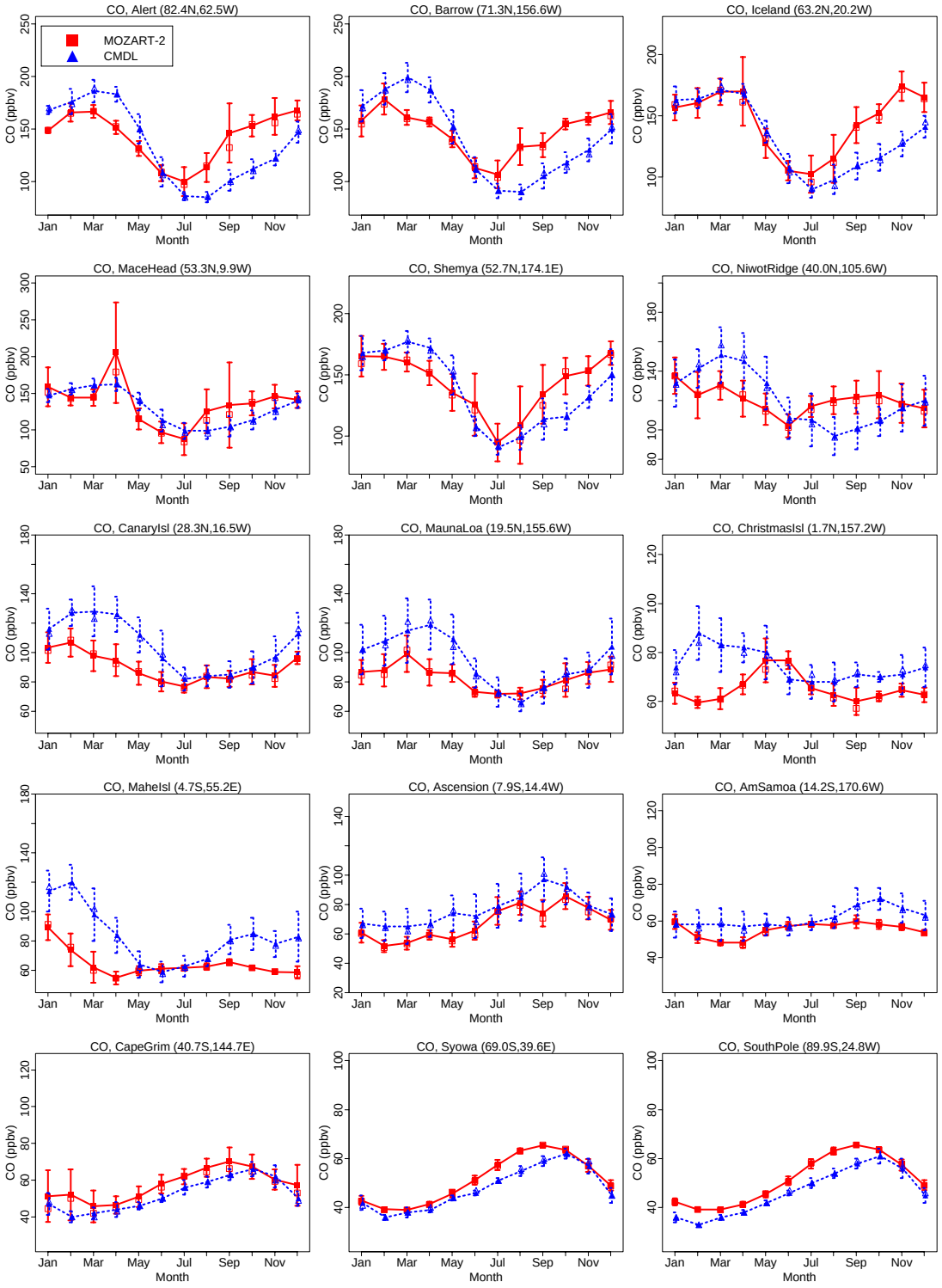

Figure 11. Comparison of observed (dotted lines) and simulated (solid lines) monthly mean carbon monoxide volume mixing ratios (ppbv) at surface sites. Observations are from the NOAA/CMDL flask measurement network [*Novelli et al.*, 1998]. Station names and locations (latitude and longitude) are given above each plot. Vertical bars indicate the standard deviations of the observations or model results within a month.

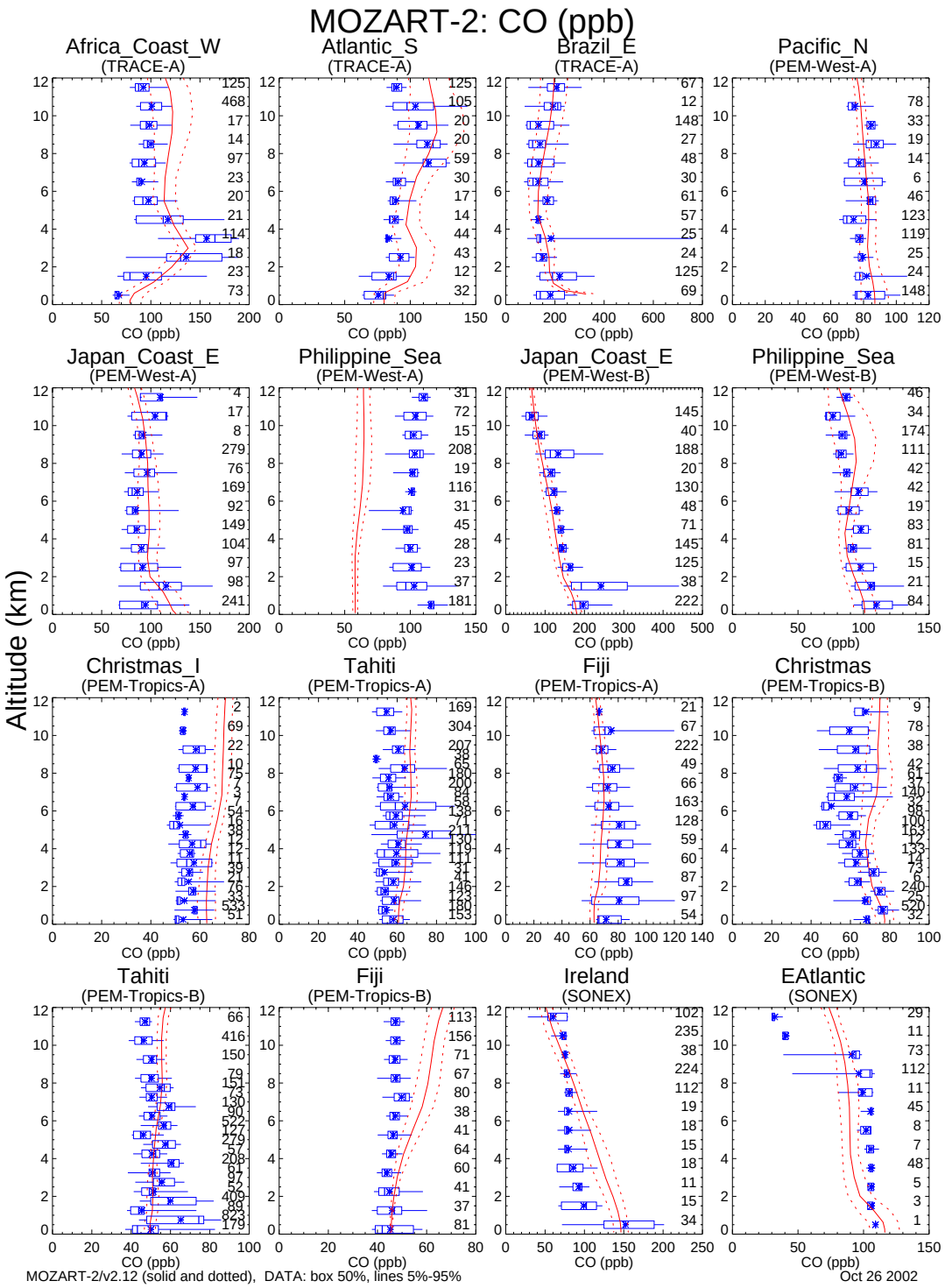

Figure 12. Same as Figure 6 but for CO (ppbv).

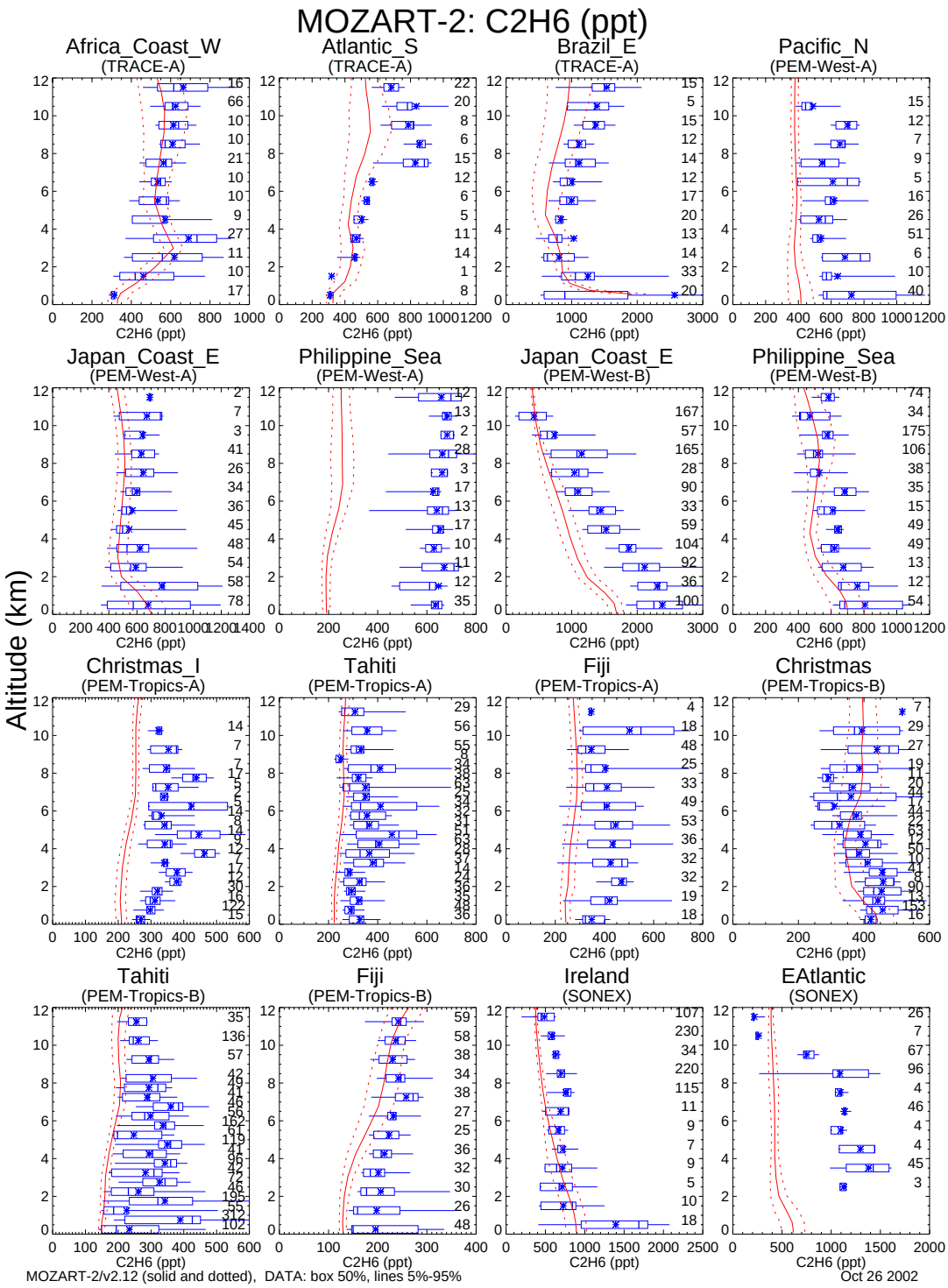

Figure 13. Same as Figure 6 but for ethane (pptv).

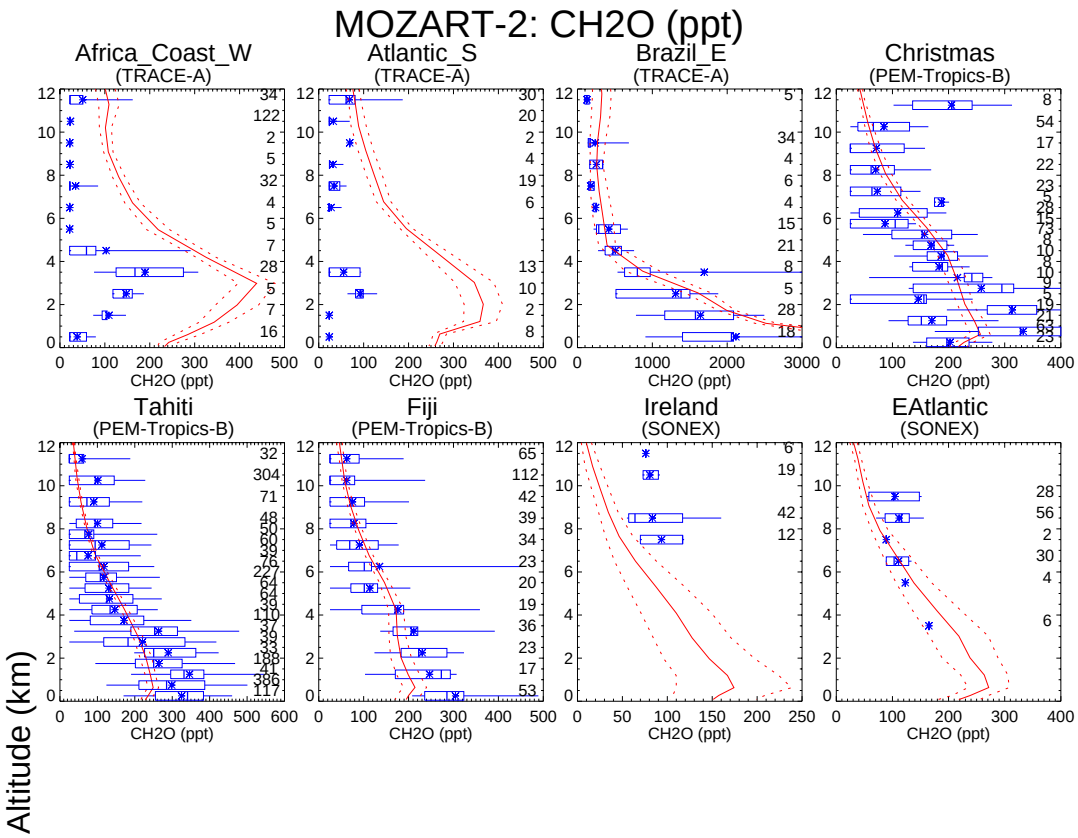

Figure 14. Same as Figure 6 but for formaldehyde (pptv).

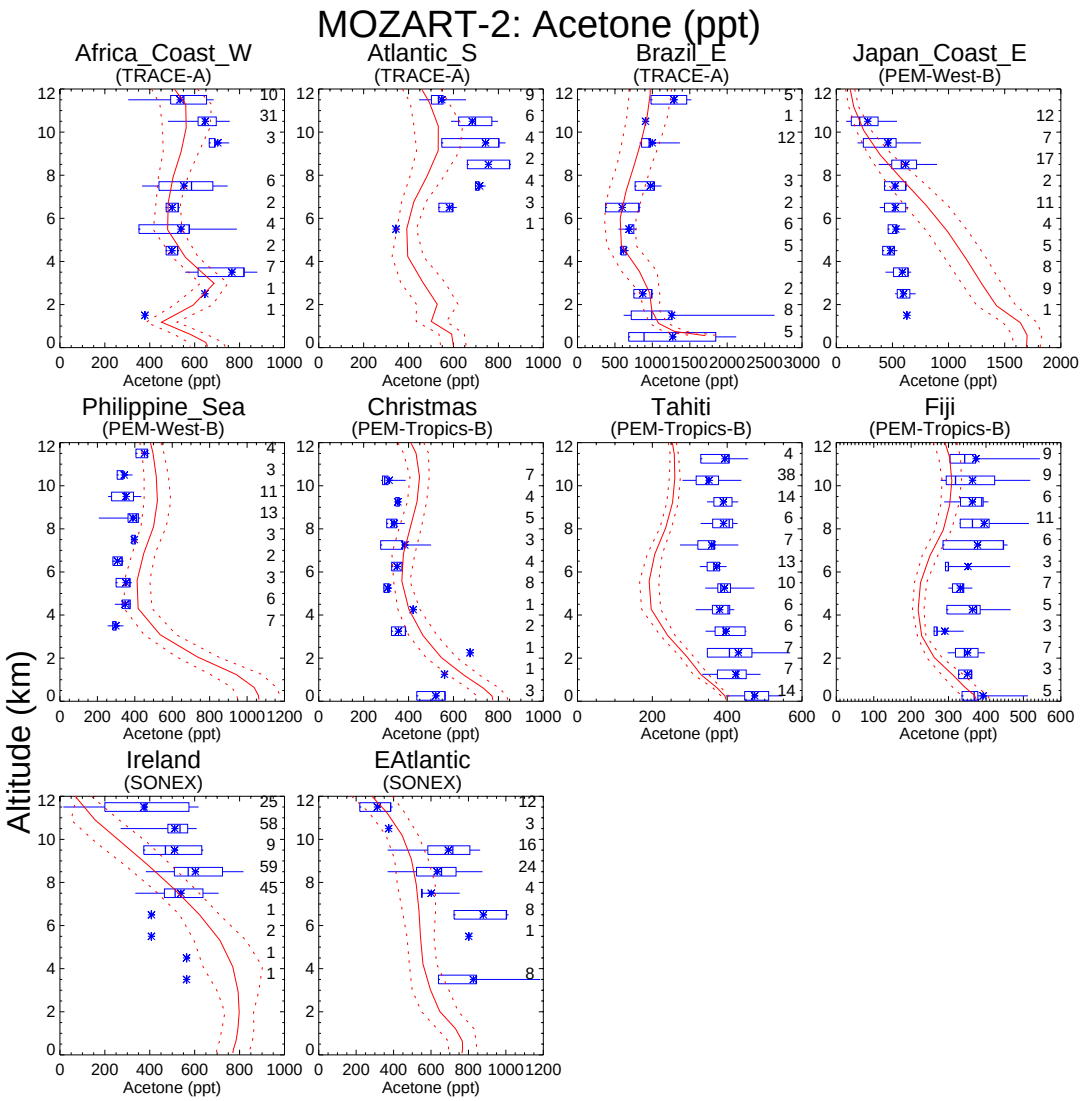

Figure 15. Same as Figure 6 but for acetone (pptv).

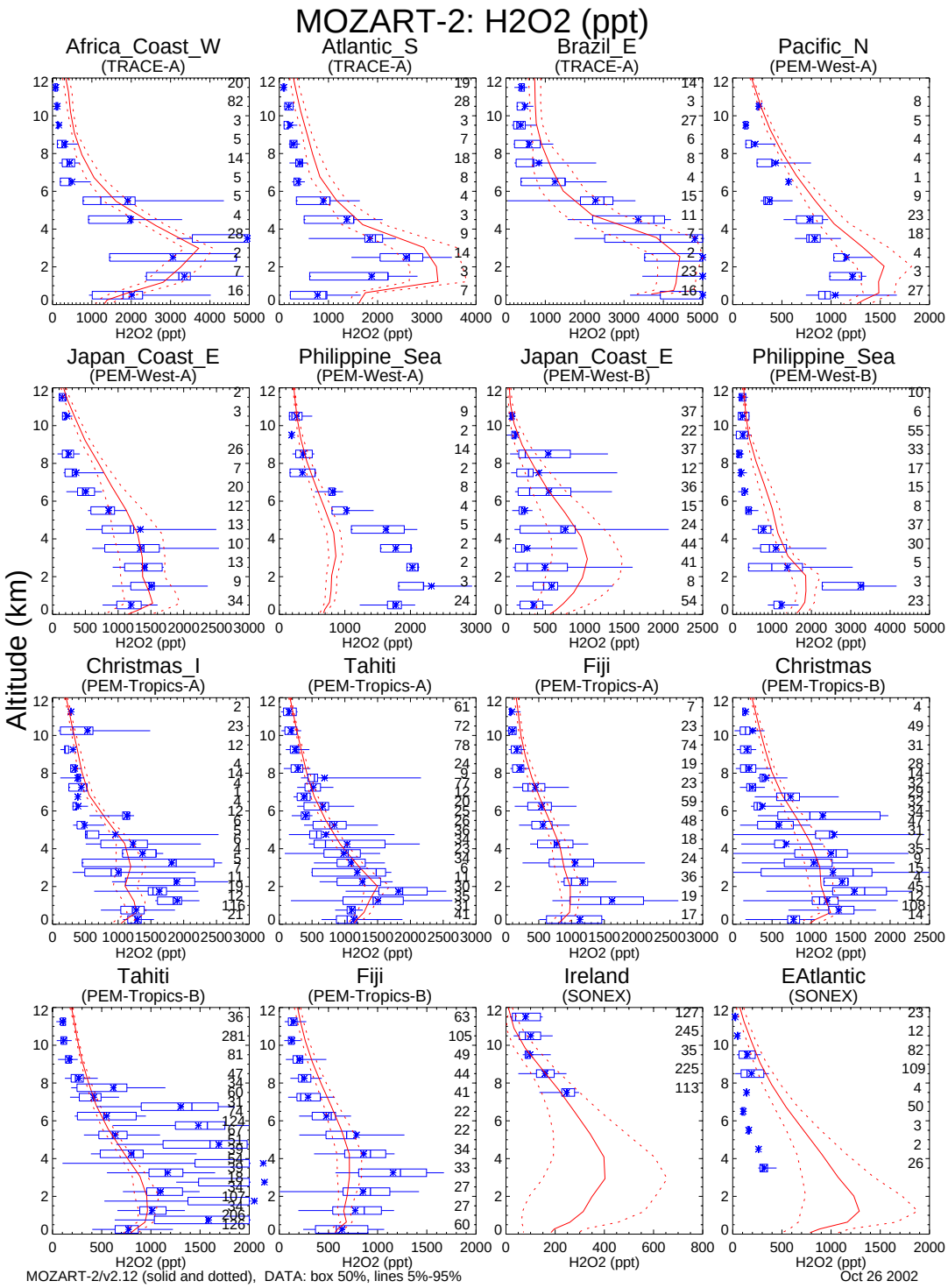

Figure 16. Same as Figure 6 but for hydrogen peroxide (pptv).

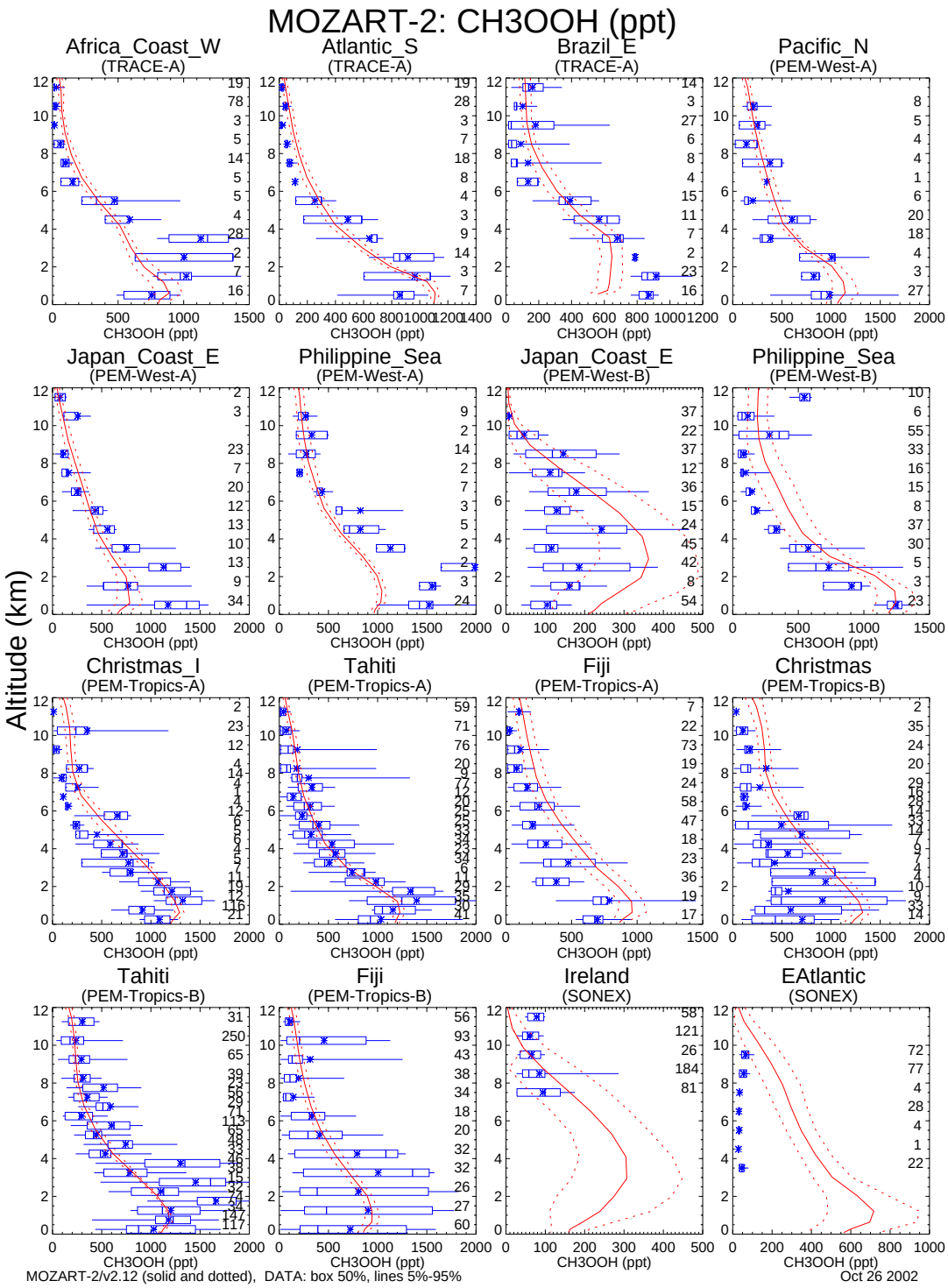

Figure 17. Same as Figure 6 but for methlyhydroperoxide (pptv).

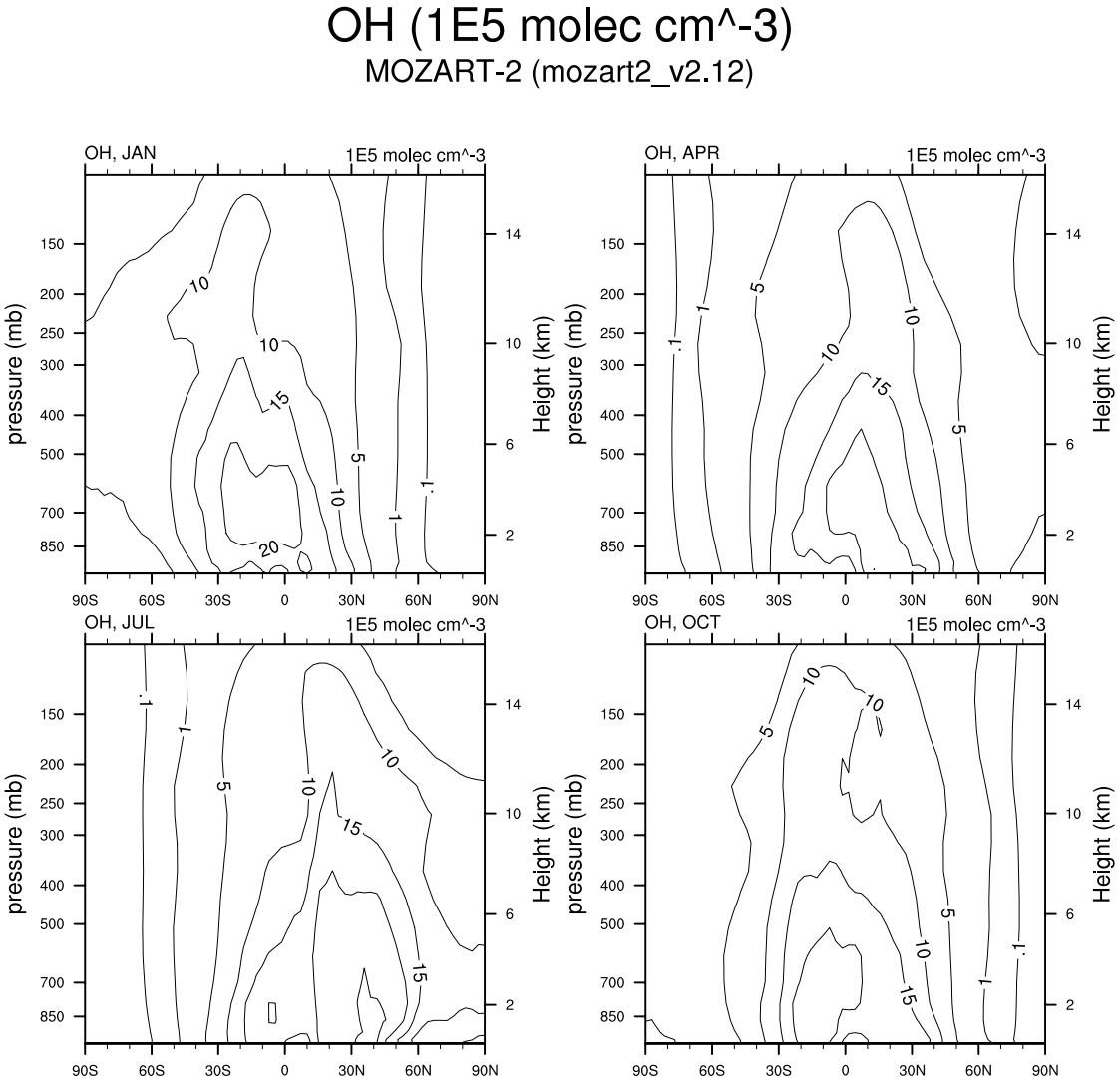

Figure 18. Zonally and monthly averaged concentrations of OH (in units of 10^5 molecules cm^{-3}) for January, April, July, and October.

Appendix A. MOZART-2 Chemical Mechanism

The chemical scheme used in MOZART-2 includes oxidation schemes for the non-methane hydrocarbons: ethane, propane, ethene, propene, isoprene, α-pinene (as a surrogate for all terpenes), and *n*-butane (as a surrogate for all hydrocarbons with 4 or more carbons, excluding isoprene and terpenes). The 63 chemical species simulated by MOZART are listed in Table A1. Kinetic reaction rates (Table A2) have been updated from those used in MOZART-1, based on recent measurements, as compiled by *Sander et al.* [2000] and *Tyndall et al.* [2001]. The isoprene oxidation mechanism has been changed considerably from the simple scheme used in MOZART-1, based on work by *Horowitz et al.* [1998], *Brocheton* [1999], and *Orlando et al.* [1999]. Heterogeneous reactions of N_2O_5 and NO_3 on sulfate aerosols are included in MOZART-2, with the sulfate aerosol distribution prescribed based on a sulfate aerosol mass simulation performed in MOZART-1 [*Tie et al.*, 2001]. Photolysis frequencies (Table A3) are computed using a precalculated multivariate interpolation table, derived from calculations conducted using the Tropospheric Ultraviolet and Visible radiation model (TUV, version 3.0) [*Madronich and Flocke*, 1998], with the quantum yield of $O(^1D)$ from photolysis of ozone updated based on *Sander et al.* [2000]. The lookup table gives clear sky photolysis frequencies as a function of pressure, overhead ozone column, solar zenith angle, surface albedo, and temperature profile. Photolysis frequencies are adjusted for cloudiness by applying a cloud correction factor, as described by *Brasseur et al.* [1998]. The chemical system is solved numerically using a fully implicit Euler backward method with Newton-Raphson iteration.

Table A1: Chemical Species in MOZART

$O_x = O_3 + O(^3P) + O(^1D)$	MACR (CH_2CCH_3CHO)
N_2O	$MACRO_2$ ($CH_3COCHO_2CH_2OH$)
N	MACROOH ($CH_3COCHOOHCH_2OH$)
NO	MCO_3 ($CH_2CCH_3CO_3$)
NO_2	$C_2H_5O_2$
NO_3	C_2H_5OOH
HNO_3	$C_{10}H_{16}$
HO_2NO_2	C_3H_8
N_2O_5	$C_3H_7O_2$
CH_4	C_3H_7OOH
CH_3O_2	CH_3COCH_3
CH_3OOH	ROOH (CH_3COCH_2OOH)
CH_2O	CH_3OH
CO	C_2H_5OH
OH	GLYALD ($HOCH_2CHO$)
HO_2	HYAC (CH_3COCH_2OH)
H_2O_2	EO_2 ($HOCH_2CH_2O_2$)
C_3H_6	EO ($HOCH_2CH_2O$)
ISOP (C_5H_8)	HYDRALD ($HOCH_2CCH_3CHCHO$)
PO_2 ($C_3H_6OHO_2$)	RO_2 ($CH_3COCH_2O_2$)
CH_3CHO	CH_3COCHO
POOH (C_3H_6OHOOH)	Rn-222
CH_3CO_3	Pb-210
CH_3COOOH	$ISOPNO_3$ ($CH_2CHCCH_3OOCH_2ONO_2$)
PAN ($CH_3CO_3NO_2$)	ONITR ($CH_2CCH_3CHONO_2CH_2OH$)
ONIT ($CH_3COCHO_2CH_2OHNO$)	XO_2 ($HOCH_2COOCH_3CHCHOH$)
C_2H_6	XOOH ($HOCH_2COOHCH_3CHCHOH$)
C_2H_4	ISOPOOH ($HOCH_2COOHCH_3CHCH_2$)
C_4H_{10}	H_2
MPAN ($CH_2CCH_3CO_3NO_2$)	stratospheric O_3
$ISOPO_2$ ($HOCH_2COOCH_3CHCH_2$)	inert O_3
MVK ($CH_2CHCOCH_3$)	

Table A2: Chemical Reactions in MOZART

Reaction	Rate Constant[a]	Refs
$O + O_2 + M \rightarrow O_3 + M$	$6.00E\text{-}34*(300/T)^{2.4}$	2
$O + O_3 \rightarrow 2*O_2$	$8.00E\text{-}12*\exp(-2060/T)$	1
$O(^1D) + N_2 \rightarrow O + N_2$	$1.80E\text{-}11*\exp(110/T)$	1
$O(^1D) + O_2 \rightarrow O + O_2$	$3.20E\text{-}11*\exp(70/T)$	1
$O(^1D) + H_2O \rightarrow 2*OH$	2.20E-10	2
$N_2O + O(^1D) \rightarrow 2*NO$	6.70E-11	2
$N_2O + O(^1D) \rightarrow N_2 + O_2$	4.90E-11	2
$NO + HO_2 \rightarrow NO_2 + OH$	$3.50E\text{-}12*\exp(250/T)$	1
$NO + O_3 \rightarrow NO_2 + O_2$	$3.00E\text{-}12*\exp(-1500/T)$	2
$NO_2 + O \rightarrow NO + O_2$	$5.60E\text{-}12*\exp(180/T)$	2
$NO_2 + O_3 \rightarrow NO_3 + O_2$	$1.20E\text{-}13*\exp(-2450/T)$	1
$NO_3 + HO_2 \rightarrow OH + NO_2$	$2.30E\text{-}12*\exp(170/T)$	1, 11
$NO_2 + NO_3 + M \rightarrow N_2O_5 + M$	$k_0=2.00E\text{-}30*(300/T)^{4.4}$ $k_\infty=1.40E\text{-}12*(300/T)^{0.7}$ F=0.60	2[b]
$N_2O_5 + M \rightarrow NO_2 + NO_3 + M$	$K_{eq} = 3.00E\text{-}27*\exp(10991/T)$	2[c]
$NO_2 + OH + M \rightarrow HNO_3 + M$	$k_0=2.40E\text{-}30*(300/T)^{3.1}$ $k_\infty=1.70E\text{-}11*(300/T)^{2.1}$ F=0.60	2[b]
$HNO_3 + OH \rightarrow NO_3 + H_2O$	$k_0=2.4E\text{-}14*\exp(460/T)$ $k_2=2.7E\text{-}17*\exp(2199/T)$ $k_3=6.5E\text{-}34*\exp(1335/T)$ $k = k_0 + \frac{k_3[M]}{1 + k_3[M]/k_2}$	2
$NO_3 + NO \rightarrow 2*NO_2$	$1.50E\text{-}11*\exp(170/T)$	1
$NO_2 + HO_2 + M \rightarrow HO_2NO_2 + M$	$k_0=1.80E\text{-}31*(300/T)^{3.2}$ $k_\infty=4.70E\text{-}12*(300/T)^{1.4}$ F=0.60	1[b]
$HO_2NO_2 + OH \rightarrow H_2O + NO_2 + O_2$	$1.30E\text{-}12*\exp(380/T)$	1
$HO_2NO_2 + M \rightarrow HO_2 + NO_2 + M$	$K_{eq} = 2.10E\text{-}27*\exp(10900/T)$	1[c]
$CH_4 + OH \rightarrow CH_3O_2 + H_2O$	$2.45E\text{-}12*\exp(-1775/T)$	1
$CH_4 + O(^1D) \rightarrow .75*CH_3O_2 + .75*OH + .25*CH_2O + .4*HO_2 + .05*H_2$	1.50E-10	1
$CH_3O_2 + NO \rightarrow CH_2O + NO_2 + HO_2$	$3.00E\text{-}12*\exp(280/T)$	1

Table A2: Chemical Reactions in MOZART (cont'd)

Reaction	Rate Constant[a]	Refs
$CH_3O_2 + CH_3O_2 \rightarrow 2*CH_2O + 2*HO_2$	5.00E-13*exp(-424/T)	6
$CH_3O_2 + CH_3O_2 \rightarrow CH_2O + CH_3OH$	1.90E-14*exp(706/T)	6
$CH_3O_2 + HO_2 \rightarrow CH_3OOH + O_2$	3.80E-13*exp(800/T)	1
$CH_3OOH + OH \rightarrow .7*CH_3O_2 + .3*OH + .3*CH_2O + H_2O$	3.80E-12*exp(200/T)	1
$CH_2O + NO_3 \rightarrow CO + HO_2 + HNO_3$	6.00E-13*exp(-2058/T)	1, 10
$CH_2O + OH \rightarrow CO + H_2O + HO_2$	1.00E-11	1
$CO + OH \rightarrow CO_2 + HO_2$	1.50E-13*(1 + .6*P_{atm})	1
$H_2 + O(^1D) \rightarrow HO_2 + OH$	1.10E-10	1
$O + OH \rightarrow HO_2 + O_2$	2.20E-11*exp(120/T)	1
$HO_2 + O \rightarrow OH + O_2$	3.00E-11*exp(200/T)	2
$OH + O_3 \rightarrow HO_2 + O_2$	1.50E-12*exp(-880/T)	2
$HO_2 + O_3 \rightarrow OH + 2*O_2$	2.00E-14*exp(-680/T)	2
$HO_2 + HO_2 \rightarrow H_2O_2$	{2.30E-13*exp(600/T) + 1.7E-33*[M]*exp(1000/T)} * (1 + 1.4E-21*exp(2200/T) * [H_2O])	1
$H_2O_2 + OH \rightarrow H_2O + HO_2$	2.90E-12*exp(-160/T)	1
$OH + HO_2 \rightarrow H_2O + O_2$	4.80E-11*exp(250/T)	2
$OH + OH \rightarrow H_2O + O$	4.20E-12*exp(-240/T)	1
$H_2 + OH \rightarrow H_2O + HO_2$	5.50E-12*exp(-2000/T)	1
$C_3H_6 + OH + M \rightarrow PO_2 + M$	k_0=8.00E-27*(300/T)$^{3.5}$ k_∞=3.00E-11 F=0.50	7[b]
$C_3H_6 + O_3 \rightarrow .54*CH_2O + .19*HO_2 + .33*OH + .08*CH_4 + .56*CO + .5*CH_3CHO + .31*CH_3O_2 + .25*CH_3COOH$	6.50E-15*exp(-1900/T)	1
$C_3H_6 + NO_3 \rightarrow ONIT$	4.60E-13*exp(-1156/T)	6
$PO_2 + NO \rightarrow CH_3CHO + CH_2O + HO_2 + NO_2$	4.20E-12*exp(180/T)	4
$PO_2 + HO_2 \rightarrow POOH + O_2$	7.50E-13*exp(700/T)	6
$POOH + OH \rightarrow .5*PO_2 + .5*OH + .5*HYAC + H_2O$	3.80E-12*exp(200/T)	4, 6
$CH_3CHO + OH \rightarrow CH_3CO_3 + H_2O$	5.60E-12*exp(270/T)	1
$CH_3CHO + NO_3 \rightarrow CH_3CO_3 + HNO_3$	1.40E-12*exp(-1900/T)	1
$CH_3CO_3 + NO \rightarrow CH_3O_2 + CO_2 + NO_2$	8.10E-12*exp(270/T)	6
$CH_3CO_3 + NO_2 + M \rightarrow PAN + M$	k_0=8.50E-29*(300/T)$^{6.5}$ k_∞=1.10E-11*(300/T) F=0.60	6[b]
$CH_3CO_3 + HO_2 \rightarrow .7*CH_3COOOH + .3*CH_3COOH + .3*O_3$	4.30E-13*exp(1040/T)	1, 12

Table A2: Chemical Reactions in MOZART (cont'd)

Reaction	Rate Constant[a]	Refs
$CH_3CO_3 + CH_3O_2 \rightarrow .9*CH_3O_2 + CH_2O + .9*HO_2 + .9*CO_2 + .1*CH_3COOH$	1.30E-12*exp(640/T)	1
$CH_3COOOH + OH \rightarrow .5*CH_3CO_3 + .5*CH_2O + .5*CO_2 + H_2O$	1.00E-12	6
$PAN + M \rightarrow CH_3CO_3 + NO_2 + M$	K_{eq} = 9.00E-29 * exp(14000/T)	6[c]
$CH_3CO_3 + CH_3CO_3 \rightarrow 2*CH_3O_2 + 2*CO_2$	2.50E-12*exp(500/T)	6
$ISOP + O_3 \rightarrow .4*MACR + .2*MVK + .07*C_3H_6 + .27*OH + .06*HO_2 + .6*CH_2O + .3*CO + .1*O_3 + .2*MCO_3 + .2*CH_3COOH$	1.05E-14*exp(-2000/T)	3, 6
$OH + C_2H_6 \rightarrow C_2H_5O_2 + H_2O$	8.70E-12*exp(-1070/T)	1
$C_2H_5O_2 + NO \rightarrow CH_3CHO + HO_2 + NO_2$	2.60E-12*exp(365/T)	1
$C_2H_5O_2 + HO_2 \rightarrow C_2H_5OOH + O_2$	7.50E-13*exp(700/T)	1
$C_2H_5O_2 + CH_3O_2 \rightarrow .7*CH_2O + .8*CH_3CHO + HO_2 + .3*CH_3OH + .2*C_2H_5OH$	2.00E-13	6
$C_2H_5O_2 + C_2H_5O_2 \rightarrow 1.6*CH_3CHO + 1.2*HO_2 + .4*C_2H_5OH$	6.80E-14	1
$C_2H_5OOH + OH \rightarrow .5*C_2H_5O_2 + .5*CH_3CHO + .5*OH$	3.80E-12*exp(200/T)	4
$OH + C_2H_4 + M \rightarrow .75*EO_2 + .5*CH_2O + .25*HO_2 + M$	k_0=1.00E-28*(300/T)$^{0.8}$ k_∞=8.80E-12 F=0.60	1[b]
$EO2 + NO \rightarrow EO + NO_2$	4.20E-12*exp(180/T)	6
$EO + O2 \rightarrow GLYALD + HO_2$	1.00E-14	6
$EO \rightarrow 2*CH_2O + HO_2$	1.60E+11*exp(-4150/T)	6
$O_3 + C_2H_4 \rightarrow CH_2O + .12*HO_2 + .5*CO + .12*OH + .32*CH_3COOH$	1.20E-14*exp(-2630/T)	1
$ISOP + OH \rightarrow ISOPO_2$	2.54E-11*exp(410/T)	3
$C_4H_{10} + OH \rightarrow 1.33*C_3H_7O_2$	1.55E-11*exp(-540/T)	5, 6
$ISOPO_2 + NO \rightarrow .08*ONITR + .92*NO_2 + HO_2 + .51*CH_2O + .23*MACR + .32*MVK + .37*HYDRALD$	2.20E-12*exp(180/T)	3, 6
$ISOPO_2 + NO_3 \rightarrow HO_2 + NO_2 + .6*CH_2O + .25*MACR + .35*MVK + .4*HYDRALD$	2.40E-12	6
$ISOPO_2 + HO_2 \rightarrow ISOPOOH$	8.00E-13*exp(700/T)	6
$ISOPO_2 + CH_3O_2 \rightarrow .25*CH_3OH + HO_2 + 1.2*CH_2O + .19*MACR + .26*MVK + .3*HYDRALD$	5.00E-13*exp(400/T)	6
$ISOPO_2 + CH_3CO_3 \rightarrow CH_3O_2 + HO_2 + .6*CH_2O + .25*MACR + .35*MVK + .4*HYDRALD$	1.40E-11	3, 6
$MVK + OH \rightarrow MACRO_2$	4.13E-12*exp(452/T)	3
$MVK + O_3 \rightarrow .8*CH_2O + .95*CH_3COCHO + .08*OH + .2*O_3 + .06*HO_2 + .05*CO + .04*CH_3CHO$	7.52E-16*exp(-1521/T)	6
$MACR + OH \rightarrow .5*MACRO_2 + .5*H2O + .5*MCO_3$	1.86E-11*exp(175/T)	3

Table A2: Chemical Reactions in MOZART (cont'd)

Reaction	Rate Constant[a]	Refs
MACR + O_3 → .8*CH_3COCHO + .275*HO_2 + .2*CO + .2*O_3 + .7*CH_2O + .215*OH	4.40E-15*exp(-2500/T)	3
$MACRO_2$ + NO → NO_2 + .47*HO_2 + .25*CH_2O + .25*CH_3COCHO + .53*CH_3CO_3 + .53*GLYALD + .22*HYAC + .22*CO	2.70E-12*exp(360/T)	6
$MACRO_2$ + NO → ONITR	1.30E-13*exp(360/T)	6
$MACRO_2$ + NO_3 → NO_2 + .47*HO_2 + .25*CH_2O + .25*CH_3COCHO + .22*CO + .53*GLYALD + .22*HYAC + .53*CH_3CO_3	2.40E-12	6
$MACRO_2$ + HO_2 → MACROOH	8.00E-13*exp(700/T)	6
$MACRO_2$ + CH_3O_2 → .73*HO_2 + .88*CH_2O + .11*CO + .24*CH_3COCHO + .26*GLYALD + .26*CH_3CO_3 + .25*CH_3OH + .23*HYAC	5.00E-13*exp(400/T)	6
$MACRO_2$ + CH_3CO_3 → .25*CH_3COCHO + CH_3O_2 + .22*CO + .47*HO_2 + .53*GLYALD + .22*HYAC + .25*CH_2O + .53*CH_3CO_3	1.40E-11	3, 6
MACROOH + OH →.5*MCO_3 + .2*$MACRO_2$ + .1*OH + .2*HO_2	2.30E-11*exp(200/T)	6
MCO_3 + NO → NO_2 + CH_2O + CH_3CO_3	5.30E-12*exp(360/T)	6
MCO_3 + NO_3 → NO_2 + CH_2O + CH_3CO_3	5.00E-12	6
MCO_3 + HO_2 → .3*O_3 + .3*CH_3COOH + .7*CH_3COOOH + .7*O_2	4.30E-13*exp(1040/T)	6
MCO_3 + CH_3O_2 → 2*CH_2O + HO_2 + CO_2 + CH_3CO_3	1.30E-12*exp(640/T)	6
MCO_3 + CH_3CO_3 → 2*CO_2 + CH_3O_2 + CH_2O + CH_3CO_3	4.60E-12*exp(530/T)	6
MCO_3 + MCO_3 → 2*CO_2 + 2*CH_2O + 2*CH_3CO_3	2.30E-12*exp(530/T)	6
MCO_3 + NO_2 (+ M) → MPAN (+ M)	1.1E-11 * (300/T)	6
MPAN + M → MCO_3 + NO_2 + M	K_{eq} = 9.00E-29 * exp(14000/T)	6
$C_{10}H_{16}$ + OH → 1.64*$ISOPO_2$ + 0.1*CH_3COCH_3	1.20E-11*exp(444/T)	5, 6
$C_{10}H_{16}$ + O_3 → 1.122*MACR + .442*MVK + .765*O + 1.156*OH + .119*C_3H_6 + 1.326*CH_2O + .323*CO + .102*HO_2	9.90E-15*exp(-730/T)	4, 6
$C_{10}H_{16}$ + NO_3 → 1.7*$ISOPO_2$ + NO_2	5.60E-11*exp(-650/T)	4
N_2O_5 → 2*HNO_3	sulfate aerosol	5
NO_3 → HNO_3	sulfate aerosol	5
N + O_2 → NO + O	1.50E-11*exp(-3600/T)	1
N + NO → N_2 + O	2.10E-11*exp(100/T)	1
C_3H_8 + OH → $C_3H_7O_2$ + H_2O	1.00E-11*exp(-660/T)	1
$C_3H_7O_2$ + NO → .82*CH_3COCH_3 + NO_2 + HO_2 + .27*CH_3CHO	4.20E-12*exp(180/T)	5, 6
$C_3H_7O_2$ + HO_2 → C_3H_7OOH + O_2	7.50E-13*exp(700/T)	5
$C_3H_7O_2$ + CH_3O_2 → CH_2O + HO_2 + .82*CH_3COCH_3	3.75E-13*exp(-40/T)	5
C_3H_7OOH + OH → H_2O + $C_3H_7O_2$	3.80E-12*exp(200/T)	5

Table A2: Chemical Reactions in MOZART (cont'd)

Reaction	Rate Constant[a]	Refs
$CH_3COCH_3 + OH \rightarrow RO_2 + H_2O$	8.80E-12*exp(-1320/T) + 1.70E-14*exp(423/T)	6
$RO_2 + NO \rightarrow CH_3CO_3 + CH_2O + NO_2$	4.20E-12*exp(180/T)	5, 6
$RO_2 + HO_2 \rightarrow ROOH + O_2$	7.50E-13*exp(700/T)	5
$ROOH + OH \rightarrow RO_2 + H_2O$	3.80E-12*exp(200/T)	5
$ONIT + OH \rightarrow NO_2 + CH_3COCHO$	6.80E-13	4, 6
$ISOP + NO_3 \rightarrow ISOPNO_3$	3.03E-12*exp(-446/T)	3
$ISOPNO_3 + NO \rightarrow 1.206*NO_2 + .794*HO_2 + .072*CH_2O + .167*MACR + .039*MVK + .794*ONITR$	2.70E-12*exp(360/T)	6
$ISOPNO_3 + NO_3 \rightarrow 1.206*NO_2 + .072*CH_2O + .167*MACR + .039*MVK + .794*ONITR + .794*HO_2$	2.40E-12	6
$ISOPNO_3 + HO_2 \rightarrow XOOH + .206*NO_2 + .794*HO_2 + .008*CH_2O + .167*MACR + .039*MVK + .794*ONITR$	8.00E-13*exp(700/T)	6
$CH_3COCHO + OH \rightarrow CH_3CO_3 + CO + H_2O$	8.40E-13*exp(830/T)	3, 6
$CH_3COCHO + NO_3 \rightarrow HNO_3 + CO + CH_3CO_3$	1.40E-12*exp(-1860/T)	3
$ONITR + OH \rightarrow .5*CO + .5*CH_2O + HYDRALD + NO_2 + HO_2$	1.50E-11	6
$ONITR + NO_3 \rightarrow HO_2 + NO_2 + HYDRALD$	1.40E-12*exp(-1860/T)	6
$OH + HYDRALD \rightarrow XO2$	1.86E-11*exp(175/T)	6
$XO_2 + NO \rightarrow NO_2 + 1.5*HO_2 + CO + .25*HYAC + .25*CH_3COCHO + .25*GLYALD$	2.70E-12*exp(360/T)	6
$XO_2 + NO_3 \rightarrow NO_2 + 1.5*HO_2 + CO + .25*HYAC + .25*CH_3COCHO + .25*GLYALD$	2.40E-12	6
$XO_2 + HO_2 \rightarrow XOOH$	8.00E-13*exp(700/T)	6
$XO_2 + CH_3O_2 \rightarrow .3*CH_3OH + HO_2 + .7*CH_2O + .4*CO + .1*HYAC + .1*CH_3COCHO + .1*GLYALD$	5.00E-13*exp(400/T)	6
$XO_2 + CH_3CO_3 \rightarrow CO + CH_3O_2 + 1.5*HO_2 + .25*HYAC + .25*CH_3COCHO + .25*GLYALD$	1.30E-12*exp(640/T)	6
$XOOH + OH \rightarrow H_2O + XO_2$	1.90E-12*exp(190/T)	6
$XOOH + OH \rightarrow H_2O + OH$	$7.69E\text{-}17 * T^2 * exp(253/T)$	6
$ISOPOOH + OH \rightarrow .5*XO_2 + .5*ISOPO_2$	3.80E-12*exp(200/T)	3, 6
$OH + CH_3OH \rightarrow HO_2 + CH_2O$	6.70E-12*exp(-600/T)	1
$OH + C_2H_5OH \rightarrow HO_2 + CH_3CHO$	7.00E-12*exp(-235/T)	1
$OH + MPAN \rightarrow .5*HYAC + .5*NO_3 + .5*CH_2O + .5*HO_2$	$k_0=8.00E\text{-}27*(300/T)^{3.5}$ $k_\infty=3.00E\text{-}11$ F=0.50	6[b]
$OH + PAN \rightarrow CH_2O + NO_3$	4.00E-14	1
$OH + HYAC \rightarrow CH_3COCHO + HO_2$	3.00E-12	6

Table A2: Chemical Reactions in MOZART (cont'd)

Reaction	Rate Constant[a]	Refs
OH + GLYALD → .8*MCO_3 + .4*CO + .6*HO_2	1.00E-11	6
Rn → Pb	2.10E-06	6

Read 6.00E-34 as 6.00×10^{-34}. T = temperature (K); [M] = atmospheric density (molecules cm^{-3}); P_{atm} = atmospheric pressure (atm); [H_2O] = water vapor denisty (molecules cm^{-3}). Reference code: 1, *DeMore et al.* [1997]; 2, *Sander et al.* [2000]; 3, *Horowitz et al.* [1998]; 4, *Müller and Brasseur* [1995]; 5, *Brasseur et al.* [1998]; 6, this work; 7, *Atkinson et al.* [1996]; 8, *Kanakidou et al.* [1991]; 9, *Zimmermann and Poppe* [1996]; 10, *Cantrell et al.* [1985]; 11, *Hall et al.* [1988]; 12, *Moortgat et al.* [1989].

a. Rate constants are given in units of s^{-1} for first-order reactions, cm^3 $molec^{-1}$ s^{-1} for second order reactions, and cm^6 $molec^{-2}$ s^{-1} for third-order reactions.

b. $$k = \frac{k_0[M]}{1 + k_0 M / k_\infty} F^{\{1 + [\log_{10}(k_0 M / k_\infty)]^2\}^{-1}}$$

c.Rate constants for dissociation reactions are calculated based on the rate constant (k_f) for the corresponding association ("forward") reaction and the equilibrium constant (K_{eq}) using: $k = k_f / K_{eq}$.

Table A3: Photolysis Reactions in MOZART

$O_2 + h\nu \rightarrow 2*O$
$O_3 + h\nu \rightarrow O(^1D) + O_2$
$O_3 + h\nu \rightarrow O + O_2$
$N_2O + h\nu \rightarrow O(^1D) + N_2$
$NO + h\nu \rightarrow N + O$
$NO_2 + h\nu \rightarrow NO + O$
$N_2O_5 + h\nu \rightarrow NO_2 + NO_3$
$HNO_3 + h\nu \rightarrow NO_2 + OH$
$NO_3 + h\nu \rightarrow .89*NO_2 + .11*NO + .89*O_3$
$HO_2NO_2 + h\nu \rightarrow NO_2 + HO_2$
$CH_3OOH + h\nu \rightarrow CH_2O + HO_2 + OH$
$CH_2O + h\nu \rightarrow CO + 2*HO_2$
$CH_2O + h\nu \rightarrow CO + H_2$
$H_2O + h\nu \rightarrow OH + HO_2$
$H_2O_2 + h\nu \rightarrow 2*OH$
$CH_3CHO + h\nu \rightarrow CH_3O_2 + CO + HO_2$
$POOH + h\nu \rightarrow CH_3CHO + CH_2O + HO_2 + OH$
$CH_3COOOH + h\nu \rightarrow CH_3O_2 + OH + CO_2$
$PAN + h\nu \rightarrow .6*CH_3CO_3 + .6*NO_2 + .4*CH_3O_2 + .4*NO_3$
$MPAN + h\nu \rightarrow MCO_3 + NO_2$
$MACR + h\nu \rightarrow .67*HO_2 + .33*MCO_3 + .67*CH_2O + .67*CH_3CO_3 + .33*OH + .67*CO$
$MVK + h\nu \rightarrow .7*C_3H_6 + .7*CO + .3*CH_3O_2 + .3*CH_3CO_3$
$C_2H_5OOH + h\nu \rightarrow CH_3CHO + HO_2 + OH$
$C_3H_7OOH + h\nu \rightarrow 0.82*CH_3COCH_3 + OH + HO_2$
$ROOH + h\nu \rightarrow CH_3CO_3 + CH_2O + OH$
$CH_3COCH_3 + h\nu \rightarrow CH_3CO_3 + CH_3O_2$
$CH_3COCHO + h\nu \rightarrow CH_3CO_3 + CO + HO_2$
$XOOH + h\nu \rightarrow OH$
$ONITR + h\nu \rightarrow HO_2 + CO + NO_2 + CH_2O$
$ISOPOOH + h\nu \rightarrow .402*MVK + .288*MACR + .69*CH_2O + HO_2$
$HYAC + h\nu \rightarrow CH_3CO_3 + HO_2 + CH_2O$
$GLYALD + h\nu \rightarrow 2*HO_2 + CO + CH_2O$